Earth and Planetary Science Letters 583 (2022) 117420

Contents lists available at ScienceDirect

Earth and Planetary Science Letters

www.elsevier.com/locate/epsl

Orbitally-paced climate change in the early Cambrian and its implications for the history of the Solar System

Tan Zhang[a,b], Yifan Li[a,b,*], Tailiang Fan[a], Anne-Christine Da Silva[c], Juye Shi[a], Qi Gao[a], Mingzhi Kuang[a], Wangwei Liu[a], Zhiqian Gao[a], Mingsong Li[d,**]

[a] School of Energy Resources, China University of Geosciences (Beijing), Beijing 100083, China
[b] Key Laboratory of Marine Reservoir Evolution and Hydrocarbon Enrichment Mechanism, Ministry of Education, China University of Geosciences, Beijing 100083, China
[c] Sedimentary Petrology Laboratory, Liège University, Sart Tilman B20, Allée du Six Août 12, 4000 Liège, Belgium
[d] Key Laboratory of Orogenic Belts and Crustal Evolution, MOE, School of Earth and Space Sciences, Peking University, Beijing 100871, China

A R T I C L E I N F O

Article history:
Received 7 July 2021
Received in revised form 22 January 2022
Accepted 6 February 2022
Available online 3 March 2022
Editor: B. Wing

Keywords:
cyclostratigraphy
sedimentary noise
Earth-Moon system evolution
Earth-Mars secular resonance
sea level
Stage 2-Stage 3

A B S T R A C T

The early Cambrian was a critical period of Earth history, marked by explosive diversification of metazoans and several profound changes in Earth's surface environments and global climate. A valid temporal framework for the early Cambrian Period and across the major bio-events is poorly constrained, and the key underlying forcings of million-year (Myr) scale sea-level variations in a greenhouse lacking polar ice sheets are still disputed. Here, the high-resolution gamma-ray logs (GR) and Fe/Al records are utilized to conduct cyclostratigraphic analysis of the early Cambrian Stage 2-Stage 3 Qiongzhusi Formation of the Well A borehole in South China. A ∼10.8 Myr-long high-resolution astronomical time scale across Stage 2-Stage 3 is developed by astronomical tuning of gamma-ray logs and Fe/Al series to the stable 405-kyr long-eccentricity cycles. The Myr-scale sea-level fluctuations in the early Cambrian greenhouse are reconstructed through the sedimentary noise modeling of the 405-tuned GR series and agree with sequence stratigraphic interpretations, lithofacies stacking patterns, and depositional environment changes. The antiphase correlation of filtered ∼1.5 Myr cycles of sedimentary noise curves with the ∼1.5 Myr obliquity modulation cycles demonstrates that the variations in land-ocean water exchange linked to changes in poleward moisture and heat transport dominated by ∼1.5 Myr obliquity modulation cycles may be a primary driver for eustasy during non-glacial early Cambrian period. A new resonance state in the early Cambrian Stage 2-Stage 3, manifested by ∼1.5 Myr eccentricity: ∼1.5 Myr obliquity, could be mainly associated with the Earth-Mars secular resonance and constrain the chaotic evolution of the Solar System in deep time. Two independent approaches are employed to reconstruct the history of Earth-Moon system characteristics, including the precession constant, the Earth-Moon distance and the day length. Our results enhance knowledge of the connection of Myr-scale sea-level variations to astronomically induced climate change under greenhouse climate and provide new empirical constraints on the chaotic motion of the Solar System and the evolution of the Earth-Moon System in deep time.

1. Introduction

The early Cambrian Period, one of the most critical intervals throughout Earth history, is characterized by the rapid evolution of the metazoan ecosystems, a prominent warm greenhouse climate, and modification of Earth's surface environments (e.g., Chen et al., 2015; Dahl et al., 2019; Hearing et al., 2018; Sperling et al., 2013). Perhaps most intriguingly, the Cambrian Stage 2 to Stage 3 witnessed mass extinction of small shelly fossils, the radiation of Niutitang Sponge Fauna (China) and Chengjiang Fauna; however, the plausible trigger and temporal details of these major biotic events are still hotly disputed (e.g., Erwin et al., 2011; Peng et al., 2020).

* Corresponding author at: School of Energy Resources, China University of Geosciences (Beijing), Beijing 100083, China.
** Corresponding author at: School of Earth and Space Sciences, Peking University, Beijing 100871, China.
E-mail addresses: zhangtan@cugb.edu.cn (T. Zhang), yifangeosci@gmail.com (Y. Li), ftl@cugb.edu.cn (T. Fan), ac.dasilva@uliege.be (A.-C. Da Silva), shijuye@cugb.edu.cn (J. Shi), gaoqi@cugb.edu.cn (Q. Gao), kuangmingzhi1125@gmail.com (M. Kuang), lwwccc@163.com (W. Liu), gzq@cugb.edu.cn (Z. Gao), msli@pku.edu.cn (M. Li).

https://doi.org/10.1016/j.epsl.2022.117420
0012-821X/

The early Cambrian timeframe is poorly constrained partly due to sparse radiometric ages, especially in the Cambrian Stage 2-Stage 3 (Peng et al., 2020). A reliable age model for the early Cambrian and across the major bio-events is critical for a refined evaluation of potential trigger and dynamic feedbacks during a crucial phase in the history of life on Earth.

The early Cambrian oceans provided the fundamental setting for the biological turnover, innovations and diversification of the metazoans. These changes in the marine environment, including oceanic oxygen level, sea surface temperature and ocean circulation, have been closely linked to sea-level changes (e.g., Kidder and Worsley, 2004; Li et al., 2016). In the early Cambrian greenhouses lacking continental ice sheets (Hearing et al., 2018), the observed major global sea-level variations (>75 m, Snedden and Liu, 2010) could not be interpreted through the classic glacio-eustasy modeling. Aquifer-eustasy's hypothesis suggests that the water-bearing potential fluctuations of groundwater aquifers governed by water mass exchanged between land and ocean may drive million-year-scale sea-level oscillations in warm intervals of Earth history (e.g., Hays et al., 1976; Li et al., 2018a; Wendler and Wendler, 2016). The poleward transfer of heat, moisture, and precipitation associated with astronomically forced meridional insolation gradient is expected to dominate the dynamic balance of aquifer charge versus discharge (Li et al., 2016; Raymo and Nisancioglu, 2003). The linkage between the third-order sea-level oscillations, changes in the groundwater reservoir, astronomical forced climate change have been further confirmed from sea-level reconstruction for the Late Cretaceous greenhouse (e.g., Omar et al., 2021; Sames et al., 2016; Wendler et al., 2016; Wendler and Wendler, 2016) and the early Triassic hothouse (Li et al., 2016). Recently, a sedimentary noise model has been developed for reconstructing sea-level fluctuations in shallow marine environments by assessing the non-orbital signal component in an orbitally tuned dataset (Li et al., 2018a). Sedimentary noise model has been successfully applied to Lower Triassic marine slope stratigraphy, Middle Triassic shallow carbonate platform in South China, and Paleogene lacustrine basins, demonstrating that it is a valuable method for inferring sea-level and lake-level fluctuations (Li et al., 2018a; Wang et al., 2020, 2022).

Earth's orbital parameters quasi-periodically oscillate and remain highly uncertain in astronomical cycles prior to 50 Ma due to the chaotic behavior of the Solar system (e.g., Laskar et al., 2011; Laskar, 1990). The most well-known secular resonances in the inner solar system involve dissipative effects of the Earth-Moon System and the Mars-Earth chaotic resonance (Hinnov, 2013; Laskar et al., 2004). Currently, interactions between Mars and the Earth are primarily characterized by the long-period modulation cycles of ∼1.2-myr obliquity and the ∼2.4-myr eccentricity (Hinnov, 2013; Laskar et al., 2004). According to the prediction of the numerical model, the current resonance model of 2:1 (i.e., ∼2.4 Myr eccentricity: ∼1.2 Myr obliquity) could be disrupted at some time (Ikeda and Tada, 2020; Ma et al., 2017; Olsen et al., 2019). Then a new resonance model of 1:1 would be formed, probably manifesting as ∼1.2 Myr eccentricity and 1.2 Myr obliquity cycles (Laskar et al., 2004). However, the temporal details of these two resonance models' secular evolution remain poorly constrained, especially in the early Paleozoic. Besides, friction-induced by tidally driven ocean currents reduces the Earth's rotation rate, slows obliquity and precession rates, and increases the Earth-Moon distance (Waltham, 2015). These resulting uncertainties hinder the identification of the Milankovitch cycles in the geologic record, and the constraint of the solar system's history in deep time. Quasi-periodic changes in orbital parameters can significantly affect Earth's climatic variations by controlling the temporal and spatial distribution of insolation received on the Earth's surface (Hinnov, 2013), and these climatic variations are "fingerprinted" and ultimately archived in geological records. Thus, astronomically-modulated climatic signals in sedimentary records provide the only evidence of the Earth-Moon system evolution and the chaotic behavior of the Solar system.

Here, cyclostratigraphic analysis is applied to the high-resolution gamma-ray logs and Fe/Al records from the Qiongzhusi Formation of South China spanning the early Cambrian Stage 2 to Stage 3. Four main objectives of the present study are: (1) to provide high-resolution geochronology for major bio-events in the "Cambrian explosion", (2) to reconstruct the sea-level changes in the early Cambrian using the sedimentary noise modeling, (3) to investigate the driver of Myr-scale sea-level oscillations in the early Cambrian greenhouse lacking permanent ice sheets, and (4) to offer geological evidence for the solar system's chaotic dynamical behavior and empirical constraints on the evolution of the Earth-Moon system in deep time.

2. Geological background

2.1. Paleogeography

The South China Block was formed by the collision of the Yangtze and Cathaysia blocks during the early Neoproterozoic Sibao-Jining Orogeny (Fig. 1, Wang and Li, 2003). South China Block has been universally depicted as an isolated craton at ca. 10°N during the early Cambrian (Fig. 1A, Yang et al., 2015). Paleogeographic reconstruction indicates that the Yangtze Block consisted of a shallow-water shelf, continental slope, and deep-water basin as the water deepened from the northwest to the southeast on the passive continental margin (Fig. 1B, Jiang et al., 2012). The Sichuan Basin is located in the shallow-water shelf area of the Yangtze Block (Fig. 1B). The lower Cambrian succession in Sichuan Basin comprises the Maidiping Formation (€1 m) and the Qiongzhusi Formation (€1q) in ascending order. The Qiongzhusi Formation unconformably overlies the Maidiping Formation due to the influence of Caledonian Orogeny (Zhong et al., 2014).

The studied Well A is located at Leshan City of southwestern Sichuan Province, situated paleogeographically in the shallow-water shelf setting. The Lower Cambrian Qiongzhusi Formation, with 358 m thickness, is subdivided into three members: (1) the Lower and Middle Member consisting principally of shale, calcareous shale and silty shale, and (2) the Upper Member predominately made of shale and argillaceous siltstone (Fig. 2). The Lower, Middle and Upper members are the focus of this study. The Qiongzhusi Formation was deposited in a shallow shelf and deep shelf environment.

2.2. Chronostratigraphy and biostratigraphy framework

The trilobites and small shelly fossils from the Qiongzhusi Formation of South China offer its broad age constraints. Six biozones, *Watsonella crosbyi* Assemblage Zone (Biozone III), Poorly fossiliferous Interzone (Biozone IV), *Sinosachites flabelliformis-Tannuolina zhangwentangi* Assemblage Zone (Biozone V), *Pelagiella subtriangulata* Taxon Range Zone (Biozone VI), *Parabadiella huio* Zone (Biozone VII) and *Wutanaspis-Eoredlichia* Assemblage Zone (Biozone VIII) were recognized in the Qiongzhusi Formation and its equivalents in South China (Fig. 2; Compston et al., 2008; Steiner et al., 2007; Zhu et al., 2019). The Biozone IV and V spanning the Lower and Middle Member of the Qiongzhusi Formation indicate a middle-late Xiaotanian Stage age (Fig. 2, Compston et al., 2008; Steiner et al., 2007; Zhu et al., 2019). The appearance of *Wutanaspis-Eoredlichia* Interval Zone (Biozone VIII) indicates an early-middle Qiongzhusian Stage age for the Qiongzhusi Fm Upper Member (Compston et al., 2008; Steiner et al., 2007; Zhu et al., 2019). A Chemical Abrasion Isotope-Dilution Thermal Ionization

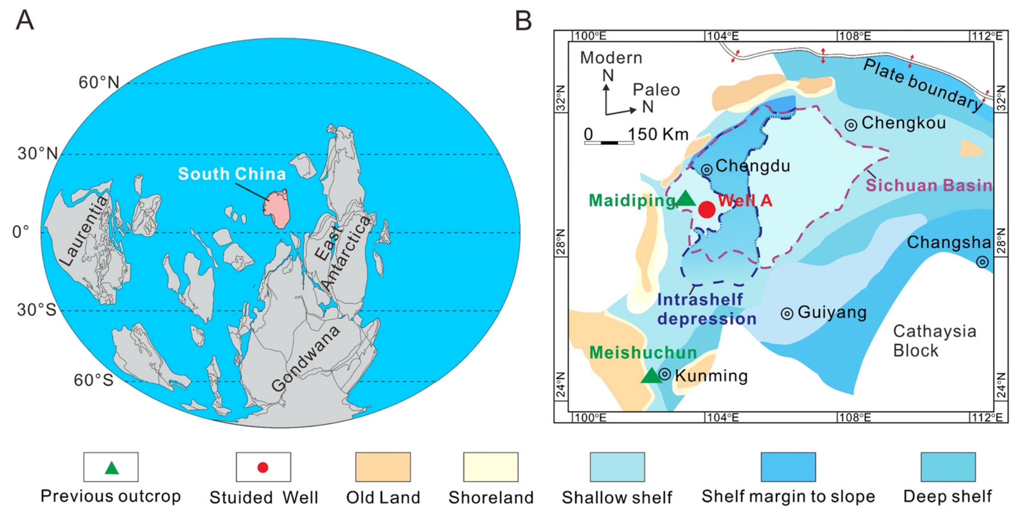

Fig. 1. (A) Global paleogeographic map of the early Cambrian Stage 3 (modified from Yang et al., 2015) shows South China's location. (B) early Cambrian paleogeography of South China (modified from Mou et al., 2012).

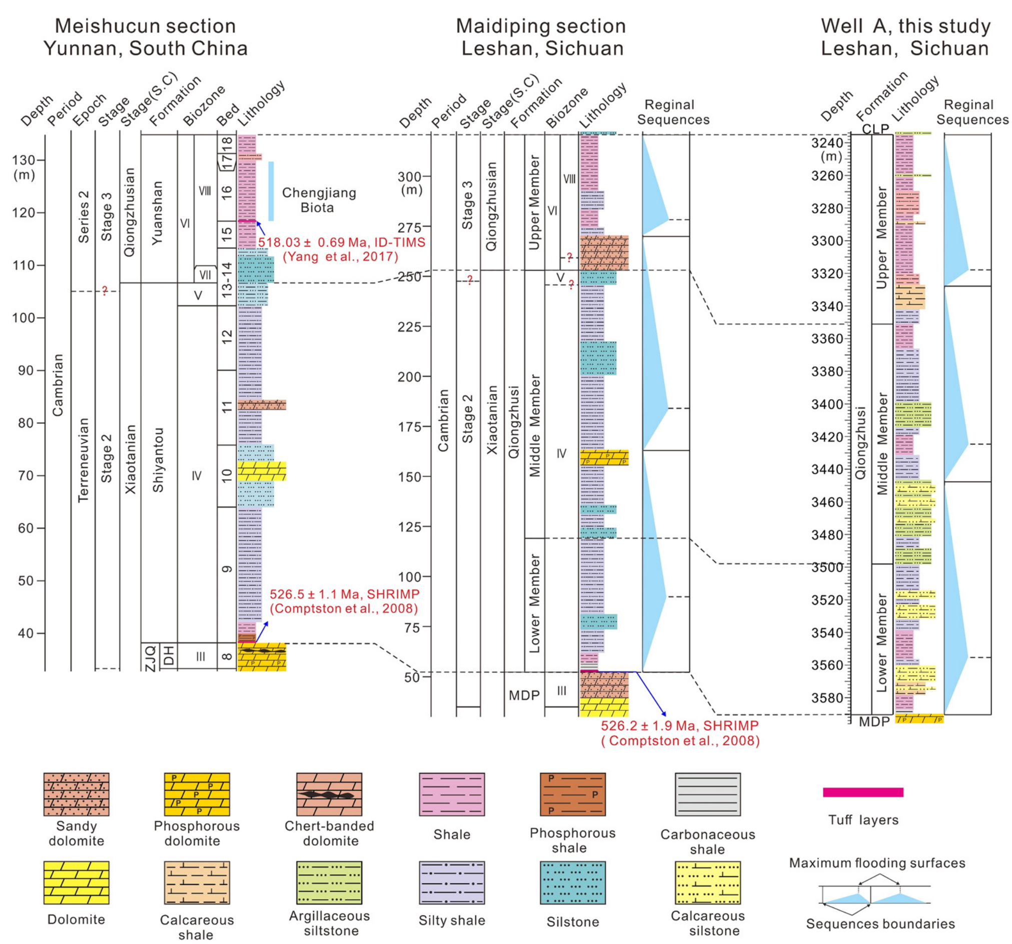

Fig. 2. Stratigraphic correlation of the Lower Cambrian successions in South China constrained by chronostratigraphy, biostratigraphy and lithostratigraphy. (A) Meishucun section; (B) Maidiping section; (C) Well A (this study). The litho-stratigraphy, radiometric dates and bed numbers from Brasier et al. (1990), Compston et al. (2008) and Yang et al. (2018); the bio-zones are from Brasier et al. (1990), Compston et al. (2008) and Steiner et al. (2007). Sequence stratigraphy of the Qiongzhusi Formation based on Liu et al. (2018). See Fig. 1B for location. The red lines represent time equivalent horizons based on lithostratigraphy and biostratigraphy. Ashes beds are marked by red bars. Biozone III= *Watsonella crosbyi* Assemblage Zone, Biozone IV= Poorly fossiliferous interzone, Biozone V= *Sinosachites flabelliformis-Tannuolina zhangwentangi* Assemblage Zone, Biozone VI= *Pelagiella subtriangulata* Taxon Range Zone, Biozone VII= *Parabadiella huio* Zone; Biozone VIII= *Wutanaspis-Eoredlichia* Assemblage Zone; ZJQ= Zhujiaqing Formation, MDP= Maidiping Formation, CLP= Canglangpu Formation, DH= Daihai Member. (For interpretation of the colors in the figure(s), the reader is referred to the web version of this article.)

Mass Spectrometry (CA-ID-TIMS) U–Pb date of 518.03 ± 0.69/0.71 Ma for the detrital zircons from the Maotianshan Shale provides the first robust maximum age of the Chengjiang biota, consistent with biostratigraphic age (Fig. 2, Yang et al., 2018). The Lower Cambrian System in South China has been regionally divided into Xiaotanian Stage, Qiongzhusian Stage, and Duyunian Stage (Zhu et al., 2019).

Cambrian Series 2 has been considered the first trilobite-dominated series, and its lower boundary has not been defined because the first appearance of the trilobites is slightly diachronous in different regions (Peng et al., 2012; Zhu et al., 2019). Trilobites recognized in Siberia (*Profallataspis jakutensis*), Morocco (*Hupetina antiqua*), and Laurenti (*Fritzaspis*) have been considered the oldest, where the first appearance datum (FAD) of trilobites is currently accepted to define the base of Stage 3 with an absolute age of 521.0 Ma (Peng et al., 2012; Zhu et al., 2019). The trilobite *Parabadiella huoi* recognized in South China is suggested to be slightly younger in age; thus, the base age of the Qiongzhusian Stage is slightly younger than 521 Ma of the International Chronostratigraphic Chart (Zhang et al., 2017; Zhu et al., 2019).

The Sensitive High-Resolution Ion Microprobe (SHRIMP) zircon U–Pb date for the bentonite has been constrained at 526.5 ± 1.1 Ma from the base of the Shiyantou Formation in the Meishucun section, consistent with a U-Pb zircon age of 526.2 ± 1.9 Ma for a thin tuff from the base of the Qiongzhusi Formation in the Maidiping section of Leshan City, Sichuan Province, coinciding with the biostratigraphy constrains (Compston et al., 2008). The Well A and the Maidiping section are geographically close (Fig. 1B) and share similar shallow marine settings and comparable lithologic successions (Fig. 2). The Qiongzhusi Formation of Well A and Maidiping section is reasonably considered age-equivalent units at the base, with an age of 526.2 ± 1.9 Ma, providing the first age constraint for our cyclostratigraphic analysis. This age constraint also points to a duration of slightly more than 5.2 ± 1.9 Myr (i.e., 526.2 ± 1.9 Ma to slightly younger than 521 Ma) for the Qiongzhusi Formation Lower and Middle Member, with a 240 m the total thickness (3391–3351 m, Fig. 2), yielding an estimated average sedimentation rate of about 3.4–7.3 cm/kyr.

3. Data and methods

3.1. Gamma-ray (GR) logging

The intensity of GR levels in sediments is related to radiogenic isotopes of potassium (K), uranium (U) and thorium (Th) contents (Schnyder et al., 2006). K, U and Th are commonly concentrated in clay and organic matter owing to their strong absorption of radioactive elements (Schnyder et al., 2006). Thus, variations in gamma-ray (GR) of sediments are mainly affected by relative clay abundance, which is actively governed by continental weathering and runoff sensitive to paleoclimate conditions (e.g., Li et al., 2017; Liu et al., 2019; Schnyder et al., 2006). Generally, increased clay-mineral inputs related to intensified hydrological cycle under warm and humid conditions could yield higher GR values (e.g., Schnyder et al., 2006; Wang et al., 2020). In contrast, reduced clay inputs under cool and dry conditions could result in lower GR values (e.g., Schnyder et al., 2006; Wang et al., 2020). Therefore, GR intensity in marine sediments, with the high signal-to-noise ratios, is one of the best proxy indicators of astronomically modulated climatic changes (Li et al., 2019b). Gamma-ray (GR) log data were collected continuously uphole within the Well A at a sampling rate of 0.125 m, covering the interval between 3233 m and 3591 m.

3.2. Geochemical proxy (Fe/Al)

Fe content reflects the enrichment of iron in the sediment when normalized against Al (i.e., Fe/Al) has proved to be a good measure of the proportion of siliciclastic sediment (Raiswell and Canfield, 2012; Wei et al., 2015). Fe/Al series can track changes in terrestrial input transported by fluvial or aeolian processes sensitive to astronomical forcing (e.g., Lamy and Hebbeln, 2000; Liu et al., 2021; Pattan et al., 2012). In Well A, geochemical data were collected at 0.1-m intervals using X-ray Fluorescence (XRF: Thermo Scientific™ Niton™ XL3t Handheld XRF Analyzer) at the drilling cores surfaces. A total of 815 geochemical data points were collected from 3480 m to 3591 m. Geochemical data were obtained at the ‘Geochemistry’ mode of the instrument (50 kV beam energies). For each measurement, individual analysis time exceeds 60 seconds, which are suggested to be sufficient to quantify the chemical composition of the sample point accurately (e.g., Saker-Clark et al., 2019; Liu et al., 2021; Sui et al., 2019).

3.3. Time series analysis

The identification and interpretation of potential astronomical-climate signals in GR and Fe/Al series within studied successions have been carried out through the following steps (1): The climate proxies were detrended by subtracting a 40-m Locally Weighted Scatterplot Smoothing (LOWESS) trend (Cleveland and Devlin, 1988). (2) Inspecting stratigraphic variable cycles was performed using evolutive Fast Fourier transform (eFFT) with a sliding window (Kodama and Hinnov, 2014). (3) The dominant frequency peaks of the detrended GR and Fe/Al data were examined by the multi-taper method (MTM) power spectrum against robust first-order autoregressive “AR(1)” red noise models (Mann and Lees, 1996) via a least squares fit of the AR(1) model to a 20% median-smoothed power spectrum. This model overcomes drawbacks in the classic AR(1) noise model that can be biased in cyclostratigraphic records (Mann and Lees, 1996), thus the robust AR(1) model becomes one the most popular approaches in cyclostratigraphic analysis. (4) The correlation coefficient (COCO) method evaluates the correlation coefficients between the power spectrum of the astronomical solution and that of the time-calibrated paleoclimate proxy series by testing a range of sediment accumulation rates (SARs) (Li et al., 2018b). The SARs with the highest COCO probably represents the optimal SAR. The variable sediment accumulation rates through studied succession were tracked by the evolutionary COCO (eCOCO) method with a sliding window (Li et al., 2018b). Therefore, our cyclostratigraphy interpretation veracity was evaluated by the optimal accumulation rate originating from COCO and eCOCO methods (Li et al., 2018b). (5) The interpreted astronomical cycles were isolated using Gaussian bandpass filtering. (6) The identified 405-kyr eccentricity-related sedimentary cycles were used for depth-to-age tuning to construct a high-resolution floating astronomical timescale. All analysis steps were performed using *Acycle* v2.4.1 software (Li et al., 2019a).

3.4. Sedimentary noise modeling

Recently, a sedimentary noise model was developed for reconstructing Myr-scale sea-level changes in marginal marine environments (Li et al., 2018a). Generally, original climate signals archived in sediments can contain much noise. Noise can be originated from punctual or cyclic events such as storms, bioturbation, or tides, from the proxy itself (e.g., proxy sensitivity and nonlinear climate responses) and other factors such as volcanism events and diagenetic alteration (Li et al., 2018a; Mudelsee et al., 2014).

In the marginal marine environment, noise associated with storms, bioturbation, tides at a fixed location is affected significantly by relative sea-level oscillation. Indeed, more intense bioturbations, storms and tide influence are expected during relatively low sea levels, leading to stronger noise. In contrast, relatively high sea level would give rise to lower sedimentary noise (Li et al., 2018a). Two complementary approaches of dynamic noise after orbital tuning (DYNOT) and lag-1 autocorrelation coefficient (ρ_1) sea-level model are involved in sedimentary noise modeling (Li et al., 2018a). DYNOT sea-level model evaluates the ratio of non-orbital signal variance to the total variance in an orbitally tuned dataset. The ρ_1 sea-level model is based on the lag-1 autocorrelation coefficient of a dataset. Both decreased DYNOT and increased ρ_1 value reflect reduced noise, corresponding to rising sea levels, and vice versa. The sample rate, window ranges, and passband cutoff frequencies used to isolate non-orbital signals are primary sources of uncertainty in these two approaches. Monte Carlo simulations were used to assess these uncertainties. A running window ranging from 400 ka and a number of 1000 is set for Monte Carlo Simulation in our uncertainty evaluation. The sedimentary noise modeling was realized using the software package *Acycle* v2.4.1 (Li et al., 2019a).

3.5. Reconstruction of the history of Earth-Moon system characteristics

Earth's dominant eccentricity periods are determined by the fundamental frequencies ("secular frequencies") of the solar system (Laskar et al., 2004), specifically the g-terms related to the orbital eccentricity and longitude of the perihelion of Mercury (g_1), Venus (g_2), Earth (g_3), Mars (g_4) and Jupiter (g_5). The precise values of Earth's five dominant eccentricity periods derive from the difference tones between these individual g terms (Laskar et al., 2004). The obliquity ($k + s_i$) and precession terms ($k + g_i$) derive from the precession constant (k) and the Solar System planetary fundamental frequencies (g_i, $i = 1, 2, 3, 4, 5$; s_i, $i = 1, 2, 3, 4, 5$; 1= Mercury, 2= Venus, 3= Earth, 4= Mars, 5= Jupiter) (Laskar et al., 2004). The precession constant k values are affected by a wide range of factors, the most important of which are Earth's rotation rate and dynamical ellipticity (e.g., Berger et al., 1992; Hinnov, 2013). Tidal dissipation of the Earth-Moon system has progressively decelerated Earth's rotation and Earth's axis precession (i.e., the precession constant, k), thereby leading to increased Earth-Moon distance and periodicities of the precession and obliquity through time (Hinnov and Hilgen, 2012; Waltham, 2015). Thus, the periods of both climate precession and obliquity change through time (Laskar et al., 2004; Waltham, 2015). Here, two independent methods, i.e., $k + s_3$ and Bayesian inversion approaches, are employed to reconstruct the precession constant k from the geological records in the early Cambrian Period.

3.5.1. $k + s_3$ approach

The relationship between precession constant k and main obliquity periodicity ($k+s_3$) has been approximated as Eq. (4) in Fang et al. (2020) (equivalent to Eq. (1) in the supplementary information, SI). The precession constant (k) also is given by Eq. (4) in Hinnov (2018) (equivalent to Eq. (2) in the SI). Dynamical ellipticity describes Earth's shape and is governed by the Earth's rotation rate, density, and gravitational and centrifugal force balances. The Eq. (9) in Berger and Loutre (1994) defined the relationship between Earth's dynamical ellipticity and Earth's rotation rate (equivalent to Eq. (3) in the SI). Earth-Moon angular momentum exchange for a range of Earth-Moon separations from today to the Roche limit has been estimated by Eq. (5) in Williams (2000) (equivalent to Eq. (4) in the SI). Firstly, we calculate the precession constant k based on Eq. (1) (see SI for detailed) using the main obliquity periodicity obtained from the cyclostratigraphic analysis. Then, using Matlab, the precession constant k is reintroduced into Eqs. (2), (3), (4), and (5) to get the Earth-Moon distance and day length (see SI for details, the codes were provided by Linda Hinnov). A detailed description of the $k + s_3$ approach is provided in the SI.

3.5.2. Bayesian inversion approach

Bayesian inversion approach (i.e., TimeOptMCMC) quantitatively establishes a connection between astronomical cycles and geologic records and directly reconstructs basic solar system frequencies, the precession constant k and astronomical cycles based on cyclostratigraphic records (Meyers and Malinverno, 2018). The TimeOpt technique, the underlying astronomical theory, and a Bayesian Markov Chain Monte Carlo methodology are the core three components that make up this approach (Meyers and Malinverno, 2018). The TimeOpt method is a statistical technique for astrochronologic testing, timescale optimization, and climate-deposition model fitting (Meyers, 2015). The methodology can increase statistical reliability in cyclostratigraphy by considering the concentration of spectrum power at predicted astronomical frequencies (Hays et al., 1976), and eccentricity-related amplitude modulation of the precession band (Shackleton et al., 1995). The TimeOpt method provides a robust framework for testing specific astronomical hypotheses based on the only optimized sedimentation rate variable by assuming that astronomical periods of the geologic archive are known, which is based on theoretical Laskar's models (Meyers, 2015). Markov Chain Monte Carlo (MCMC) simulation quantitatively evaluates prior and posterior uncertainties between the data and model space that include fundamental solar system secular frequencies g_1 to g_5, precession constant k, and sedimentation rate (Meyers and Malinverno, 2018). Bayesian inversion of the Qiongzhusi Fe/Al record is constrained by prior distributions for the fundamental frequencies g_1 to g_5 ($g_1 = 5.525 \pm 0.125$ arcsec/y, $g_2 = 7.455 \pm 0.015$ arcsec/y, $g_3 = 17.3 \pm 0.150005$ arcsec/y, $g_4 = 17.85 \pm 0.15$ arcsec/y, $g_5 = 4.257455 \pm 0.00002$ arcsec/y) representing midpoint values from Laskar et al. (2004) 500 My long simulations, and the precession constant k ($k = 59.17 \pm 5.62$ arcsec/y, at $\sim$524 Myr) from the Waltham (2015) (see SI for more detail, Tables S2). Ultimately, TimeOptMCMC reconstructed a reasonable range of values for fundamental frequencies (g terms) and precession constant k in the early Cambrian period from the Qiongzhusi Fe/Al record. Then, the precession constant k value is utilized to calculate the Earth-Moon distance and length of day using MATLAB codes (e.g., Fang et al., 2020; Huang et al., 2020). All analyses in the Bayesian inversion approach were performed using the free software v4.1.0 (R Core Team, 2021), and the implementation of the TimeOptMCMC algorithm is provided *Astrochron* package v1.0 (Meyers, 2021).

4. Results

4.1. Time series analysis

The MTM power spectrum of the GR series through the whole Qiongzhusi Formation shows significant periods (>95% confidence level) of 61.4 m, 17.1-11.9 m, 4.8-2.7 m, 2.3-1.1 m wavelengths (Fig. 3). The Upper Member GR series's power spectrum display significant peaks at wavelengths of 10.9 m, 2.7-2.0 m, and 1.8-0.94 m (Fig. 4A and D). The MTM power spectrum of the Lower and Middle members GR series is characterized by cyclic variations with wavelengths of 28.6 m, 18.9-11.9 m, 4.7-2.7 m, and 2.1-1.1 m (Fig. 4B and E). Fe/Al records from 3480 to 3591 m are characterized by 13.5 m, 5.3-2.9 m, 0.98-0.79 m, and 0.71-0.54 m wavelengths (Fig. 4C and F and Fig. S5).

The COCO sedimentation rate map of the Fe/Al series shows peaks at 3.2 cm/kyr and 3.6 cm/kyr (Fig. 5A). The COCO analysis of the whole Qiongzhusi Fm GR series displays several peaks at 2.2 cm/kyr, 2.9 cm/kyr, 4.5 cm/kyr and 5.1 cm/kyr (Fig. 5B). All of these sedimentation rates have null hypothesis (H_0) significance levels of less than 0.1% (Fig. 5). Given the estimated average accumulation rates of ca. 3.4-7.3 cm/kyr for the Lower and Middle Members constrained by independent age data (see Section 2.2),

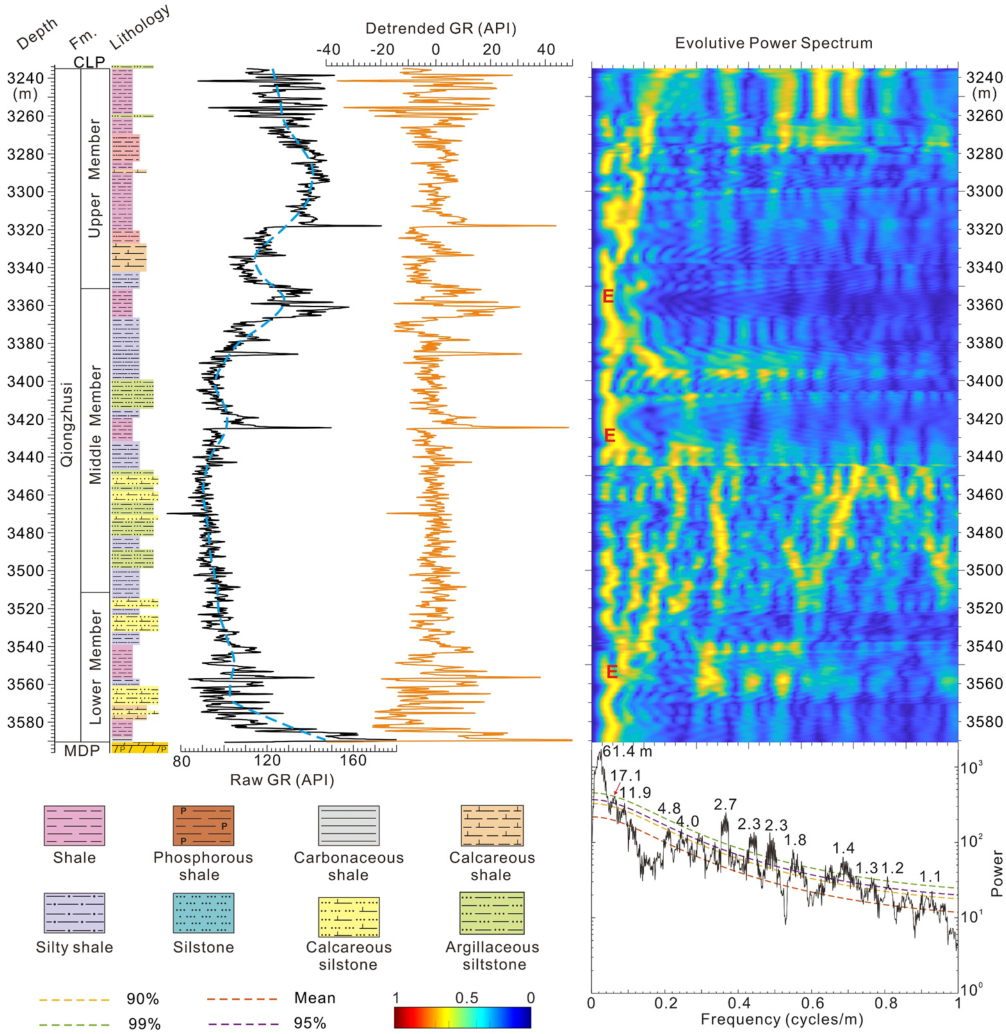

Fig. 3. Cyclostratigraphy of the Qiongzhusi Formation of Well A in South China. Qiongzhusi Formation GR series (3233-3591 m) of Well A. GR data (black line) is shown with its 40-m lowess trend (blue dotted line) and detrended GR (orange line). Evolutionary power spectrum was calculated using a 40-m running window with a 0.632 m step. 4π MTM power spectrum is shown with median, 90%, 95%, and 99% confidence levels. MDP= Maidiping Formation, CLP= Canglangpu Formation.

we can consider the optimal mean sedimentation rate of the whole Qiongzhusi Fm is 2.2-5.1 cm/kyr. Moreover, all of these optimal mean sedimentation rates are supported by the 2-6 cm/kyr indicated by eCOCO for the whole Qiongzhusi Fm (Fig. 5B).

According to the optimal mean accumulation rates of 2.2-5.1 cm/kyr constrained by COCO and eCOCO results as well as independent age data, the detected cycles were assigned to specified astronomical parameters. This yields tentative durations of 370 to 540 kyr for 18.9-m to 11.9-m cycles, 92 to 123 kyr for 4.7-m to 2.7-m cycles and 21 to 52 kyr for 2.1-m to 1.1-m cycles in the Lower and Middle Member. Thus, the 18.9-11.9 m, 4.7-2.7 m, and 2.1-1.1-m cycles of the Lower and Middle Member broadly correspond to 405-kyr long-eccentricity, the ~100-kyr short-eccentricity, and the ~30-kyr obliquity, and ~19-kyr precession periods, respectively. The 10.9 m, 2.7-2.0 m and 1.8-0.94 m cycles of the Upper Member may correspond to 405-kyr long-eccentricity, the ~100-kyr short-eccentricity, and the ~30-kyr obliquity cycles, respectively (Fig. 4). Based on the average sedimentation rate of 3.2 -3.6 cm/kyr estimated by COCO, the 13.5 m, 5.3-2.9 m, 0.98-0.79 m, and 0.71-0.54 m cycles of Fe/Al records from 3480 to 3591 m are assigned tentative durations of 420 to 375 kyr, 160 to 80 kyr, 30 kyr to 22 kyr, and 22 kyr to 15 kyr, respectively (Fig. 4). These periodicities broadly correspond to the 405- kyr long-eccentricity, the ~100-kyr short-eccentricity, the ~30-kyr obliquity, and the ~19-kyr precession cycles, respectively.

4.2. Tuning and age model

The ~14.9 m cycles of the Lower and Middle Member, the ~11.6 m cycles of the Upper Member, and the ~14.1-m cycles of the Fe/Al series from 3480 to 3591 m are isolated using the Gaussian bandpass filtering (Fig. 4). These filtered cycles are tuned using the 405-kyr long-eccentricity cycle providing a ~10.8-Myr floating astronomical time scale (ATS) for the Qiongzhusi Fm (Fig. 6A). An absolute ATS can be constructed by fixing the floating ATS to the base age of 526.2 ± 1.9 Ma at the Qiongzhusi Formation (see Section 2). The MTM power spectrum of the 405-kyr tuned GR series of the entire Qiongzhusi Fm displays significant peaks at periods of ~1.3 Myr, 610 kyr, 405 kyr, 131–114 kyr, 67.8–58.9 kyr, 47.5 kyr, all with confidence levels above 95%, while the 37.7 kyr, 31.9-29.3 kyr and 27.5 kyr cycles are weakly expressed (Fig. 6B). The power spectrum of the tuned Fe/Al series from 3480 to 3591 m has significant peaks at 405 kyr, 159 kyr, 33.5 kyr, 29.7 kyr, 24.7 kyr, 22.7 kyr, 19.8 kyr, 18.3 kyr and 14.7 kyr, all with confidence levels above 99%, while the 116 kyr and 97 kyr cycles are weakly expressed (Fig. 6C).

4.3. Sedimentary noise model for sea-level changes

Variations in sedimentary noise of the tuned GR series through the Qiongzhusi Fm are tracked using the DYNOT and ρ_1 models.

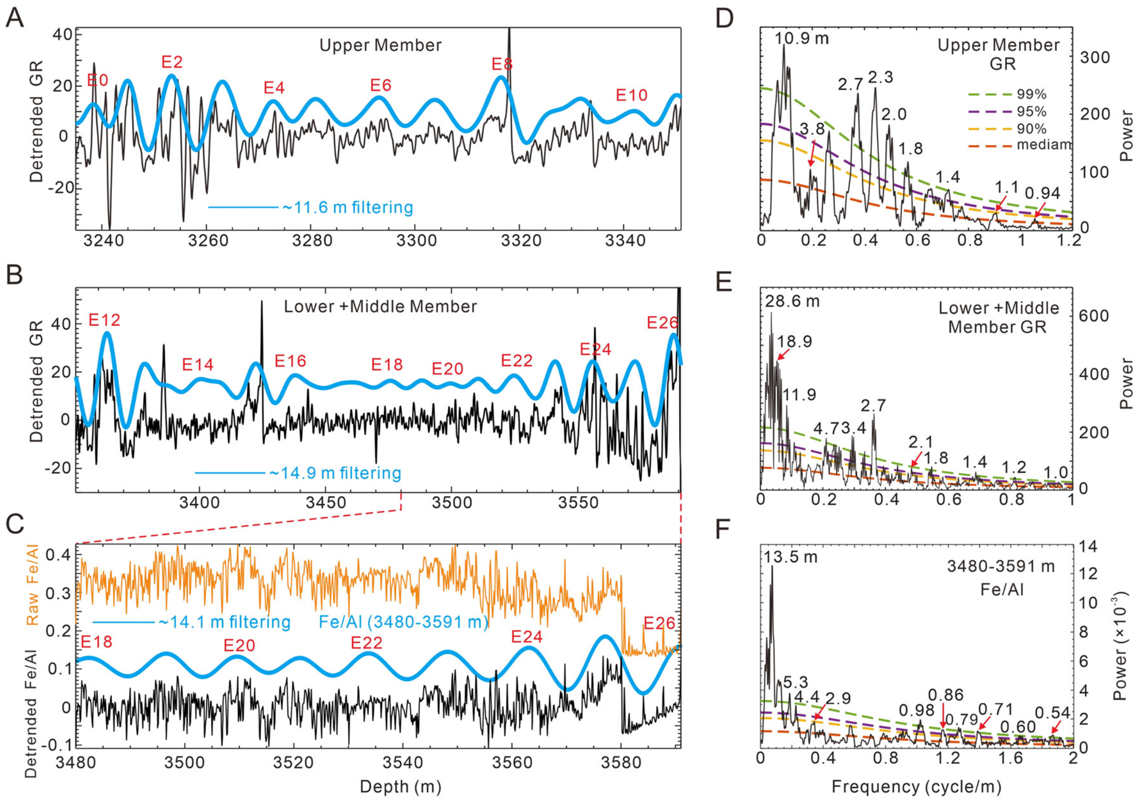

Fig. 4. Detrended GR series (left) of three members of the Qiongzhusi Fm. shown with interpreted long- (blue, 405 kyr) eccentricity cycles and their corresponding MTM power spectrum with confidence levels (right). (A) GR series of Upper Member (3235-3351 m) is shown with filtered ∼11.6 m cycles (Gaussian filter, passband: 0.086 ± 0.02 cycles/m). (B) GR series of Lower and Middle Member (3351-3591 m) is shown with ∼14.9 m cycles (Gaussian filter, passband: 0.067 ± 0.015 cycles/m); (C) Raw Fe/Al series (orange line) (3480-3591 m) is shown with detrended Fe/Al (black line) and filtered ∼14.1-m cycles (Gaussian filter, passband: 0.071 ± 0.016 cycles/m). GR series and Fe/Al records were detrended by removing a 40-m lowess trend. (D), (E) and (F) are 2π MTM power spectrum of GR and Fe/Al series in (A), (B), and (C), respectively.

Two sedimentary noise curves present similar patterns, with pronounced increased sedimentary noise in six intervals (gray bars in Fig. 7). Spectrum analysis of both the DYNOT and ρ_1 series shows significant peaks at 4.48 Myr, 2.99-2.15 Myr, 1.63-1.45 Myr, and 1.05-0.93 Myr (Fig. 8F and G). The MTM power spectrum of obliquity variance/total variance (O/T) displays significant long-term modulations cycles at 3.59 Myr, 2.07 Myr, 1.54 Myr, and 1.03 Myr (Fig. 8H).

5. Discussion

5.1. The astronomical timescale of the early Cambrian epoch

According to the astronomical time scale (ATS) defined by our cyclostratigraphic analysis, the total duration of the Qiongzhusi Formation is 10.79 ± 0.2 Myr, from 526.2 ± 1.9 to 515.41 ± 1.91 Ma. Our age model has two sources of uncertainty: (1) uncertainty of 1.90 Ma from the SHRIMP U-Pb dating for the tuff in the base Qiongzhusi Formation, (2) the subjective uncertainty of 0.2-Myr derived from the 405-kyr cycle counting. Thus, the two sources of uncertainty imply a total uncertainty of 1.91 Myr (obtained from $\sqrt{1.90^2 + 0.20^2}$) for our absolute ATS. Consequently, the age of the top Lower Member, Middle Member and Upper Member are constrained at 524.16 ± 1.91 Ma, 520.11 ± 1.91 Ma and 515.41 ± 1.91 Ma, respectively (Fig. 6A). Our astrochronology suggests a total duration of 6.09 ± 0.20 Myr for the poorly fossiliferous Zone and the *Sinosachites flabelliformis-Tannuolina zhangwentangi* Assemblage Zone (Fig. 6A). We estimate the duration of the *Pelagiella subangulata* Taxon Range Zone at 4.70 ± 0.20 Myr (Fig. 6A).

The base of the Upper Member is also the base of the Qiongzhusian Stage, which is defined by the FAD of the trilobites *Parabadiella huoi* (Section 2.2, Peng et al., 2020; Zhang et al., 2017; Zhu et al., 2019). Thus, the FAD of the trilobites *Parabadiella huoi* in South China is astrochronologically constrained at 520.11 ± 1.91 Ma (Fig. 6A). Although there is still some controversy over the taxonomic between *Parabadiella* in South China and *Abadiella* in Australia, and *Abadiella* in Morocco (Zhang et al., 2017), the earliest occurrences of trilobites currently in South China (*Parabadiella*) and in Australia (*Abadiella*) are considered younger than those in Siberia (*Profallotaspis jakutensis* and *Profallotaspis tyusserica*; Shergold et al., 1991; Varlamov et al., 2008), the western Laurentia (*Fritzaspis generalis* and *Profallotaspis?sp*; Hollingsworth, 2011, 2007), and Morocco (*Eofallotaspis tioutensis* and *Hupetina antiqua*; Geyer, 1996; Geyer et al., 1990). Few chronological constraints are reported for the first appearance of trilobites. The tuff from the upper part of the Lie de vin Formation in Morocco yielded a zircon $^{206}Pb/^{238}U$ age of 520.93 ± 0.14 Ma (Maloof et al., 2010), providing the first maximum age constrain on the earliest occurrences of trilobites in this region (Geyer and Landing, 2006). The occurrence of the first trilobites in Avalonia is roughly constrained by a zircon U–Pb age of 519.30 ± 0.23 Ma from the Caerfai Bay Shales Formation in Wales (Harvey et al., 2011). Collectively, these currently geochronological constraints possibly bracketed the occurrence of the first trilobites on different paleocontinents between 520.93 ± 0.14 Ma and 519.30 ± 0.23 Ma, including in Morocco, Avalonia and South China. Our astrochronology for the early Cambrian Qiongzhusi Formation seems to support that the earliest trilobites currently on separate paleocontinents are endemic and diachronic (Landing et al., 2013; Zhang et al., 2017). The first trilobite occurrence is one of the most striking biotic events in metazoans radiation and also signaled the onset of the major phase of the Cambrian explosion (Zhang et al., 2017, 2014). Hence, our age

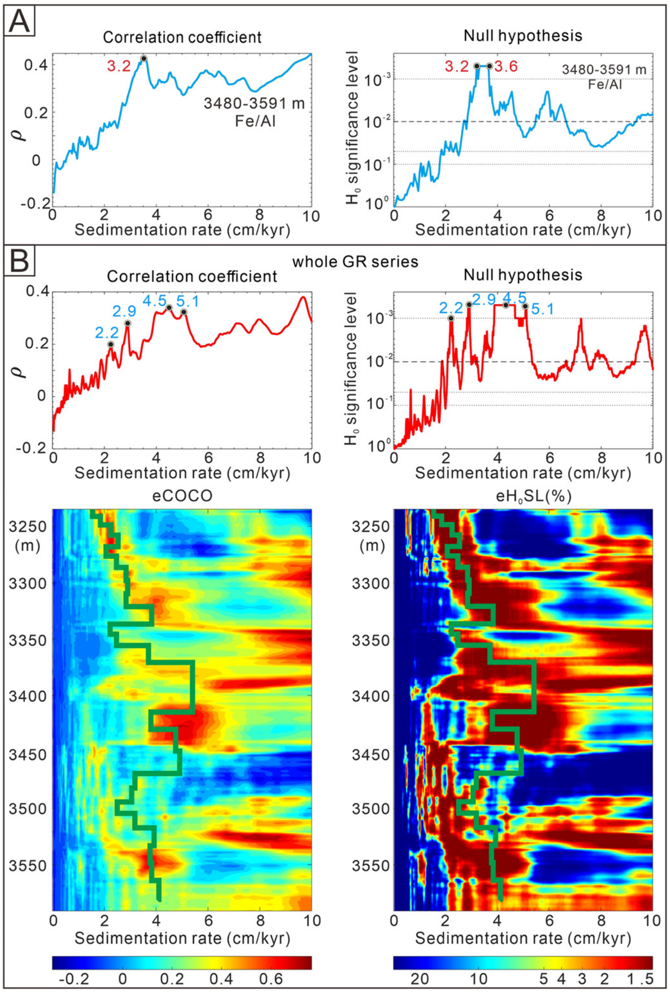

Fig. 5. (A) COCO of Fe/Al data from 3480 to 3951 m; (B) COCO and eCOCO sedimentation rate map of the whole GR series. For both the COCO and eCOCO analysis, testing sedimentation rates range from 1 to 10 cm/kyr with a step of 0.01 cm/kyr, and the number of Monte Carlo simulations is 2000. For eCOCO analysis, the sliding window is 40 m, with a sliding window step of 2 m. The thick green line within the eCOCO result is sedimentation rates according to the 405-kyr tuning of the longest (∼14.9-11.6 m) statistically prominent cycles.

model allows an increased understanding of the modernization of ecological communities in the Cambrian explosion.

5.2. Verification of sedimentation noise model for reconstructing sea levels

The early Cambrian sea-level changes revealed by the sedimentary noise model are supported by evidence from sedimentology (i.e., third-order sequence stratigraphy and lithofacies stacking patterns). These enhanced noise intervals are associated with changes in lithofacies from shale and silty shale to calcareous siltstone and argillaceous siltstone indicative of shallowing sea levels, as well as the sequence boundaries (Liu et al., 2019; gray bars, Fig. 7). In a relatively shallow shelf environment of Qiongzhusi Fm., signal-to-noise ratios in the eCOCO map could be significantly affected by sea-level oscillations. Generally, decreased signal-to-noise ratios (gray bars in Fig. 7) are characterized by the repeated discontinuities at the eCOCO map, indicating increased depositional environment instability in low sea level times (Wang et al., 2020). These apparent discontinuities recognized from the eCOCO sedimentation rates map correspond well to the high sedimentary noise interval at the DYNOT and ρ_1 curves (gray bar, Fig. 7). In addition, we test the efficacy of the sedimentary noise model (DYNOT and ρ_1) based on a synthetic GR series (follows Li et al., 2018a; See SI for more detail). The ∼1.5 Myr climate cycles in the DYNOT and ρ_1 are independent and could not arise in another random data set treated with the same filter based on our synthetic GR data analysis (See SI).

The early Cambrian sea-level curves in South China estimated by DYNOT and ρ_1 models show similar trends with contemporaneously major global eustatic events reconstructed from marine depositional sequences, demonstrating the global nature and synchronicity of these million-year scales sea-level oscillations (Fig. 8, Snedden and Liu, 2010). Minor discrepancies between the noise model and the eustatic curve may be associated with short-term tectonic activity and/or our time resolution (10^4 to 10^6 years) of the objective sedimentary noise model are much higher than the subjective reconstruction by Snedden and Liu (2010). However, the tectonic activity generally processes larger than the astronomical time scale (10^4 to 10^6 years); therefore, the latter is the preferred interpretation.

Moreover, non-astronomical noise induced by large volcanism may be additional sedimentary noise sources (Li et al., 2018a; Wang et al., 2020). The reported regions affected by volcanism during the early Cambrian were mainly located at the deep-water shelf and deep ocean basin in the southeastern part of Yangtze Block (Yin et al., 2017; Zhu et al., 2021). No evidence of large volcanic activity in the Sichuan Basin, situated at the northeastern part of Yangtze Block, where Well A is situated, has so far been reported during the early Cambrian. Thereby, noise estimation of studied successions is unlikely to have been affected by these potential noise sources (i.e., short-term tectonic activity and volcanic events).

5.3. Obliquity-forced eustasy during the early Cambrian greenhouse

Power spectrum of the detrended DYNOT and ρ_1 median curves display a main periodicity of 1.49-1.63 Myr with subordinate periodicities of 4.48-2.15 Myr and 1.05-0.93 Myr (Fig. 8F, G). The 3.59 Myr, 2.07 Myr, 1.54 Myr, and 1.03 Myr long obliquity cycles identified in the O/T series may correspond to these long-term cycles in sedimentary noise curves (Fig. 8H), implying a causal link between long-term obliquity forcing and million-year scale sea-level changes. The long-period orbital cycles have been well identified in sediments of Cenozoic (e.g., Boulila et al., 2011; Liu et al., 2019), Mesozoic (i.e., Ikeda and Tada, 2020; Ma et al., 2017; Olsen et al., 2019), and Paleozoic (e.g., Fang et al., 2019; Wu et al., 2019). Notably, it has previously been shown that global sea-level oscillation under both the Cenozoic icehouse and Mesozoic greenhouse conditions is increasingly recognized as connected to global climate change forced by long-term orbital cycles (e.g., Boulila et al., 2011; Gale et al., 2002; Li et al., 2018a; Wang et al., 2020, 2022).

Two models have been considered as forcing mechanisms for sea-level changes, i.e., glacio-eustasy (Miller, 2005) and aquifer-eustasy (Hay and Leslie, 1990), both of which are governed by the imbalanced exchange of water between continents and oceans associated with the intensity of the global hydrological cycle (e.g., Li et al., 2018a, 2016; Sames et al., 2016; Wendler et al., 2016). During icehouse states, high-amplitude sea-level variations can be explained by the retreat and advance of polar ice caps as a function of the obliquity-related insolation variation at high latitudes (e.g., Hays et al., 1976; Huybers and Wunsch, 2005; Naish et al., 2009). Aquifer-eustasy model suggests that variations in land-ocean water exchange related to the imbalance of aquifer charge versus discharge may be a primary driver of million-year-scale sea-level oscillations under the early Cambrian warm climate. However, the aquifer eustasy model raises two complications: (1) the total water storage of aquifers should be sufficient to lead to tens to hundreds of meters sea-level changes and (2) the drivers responsible for a

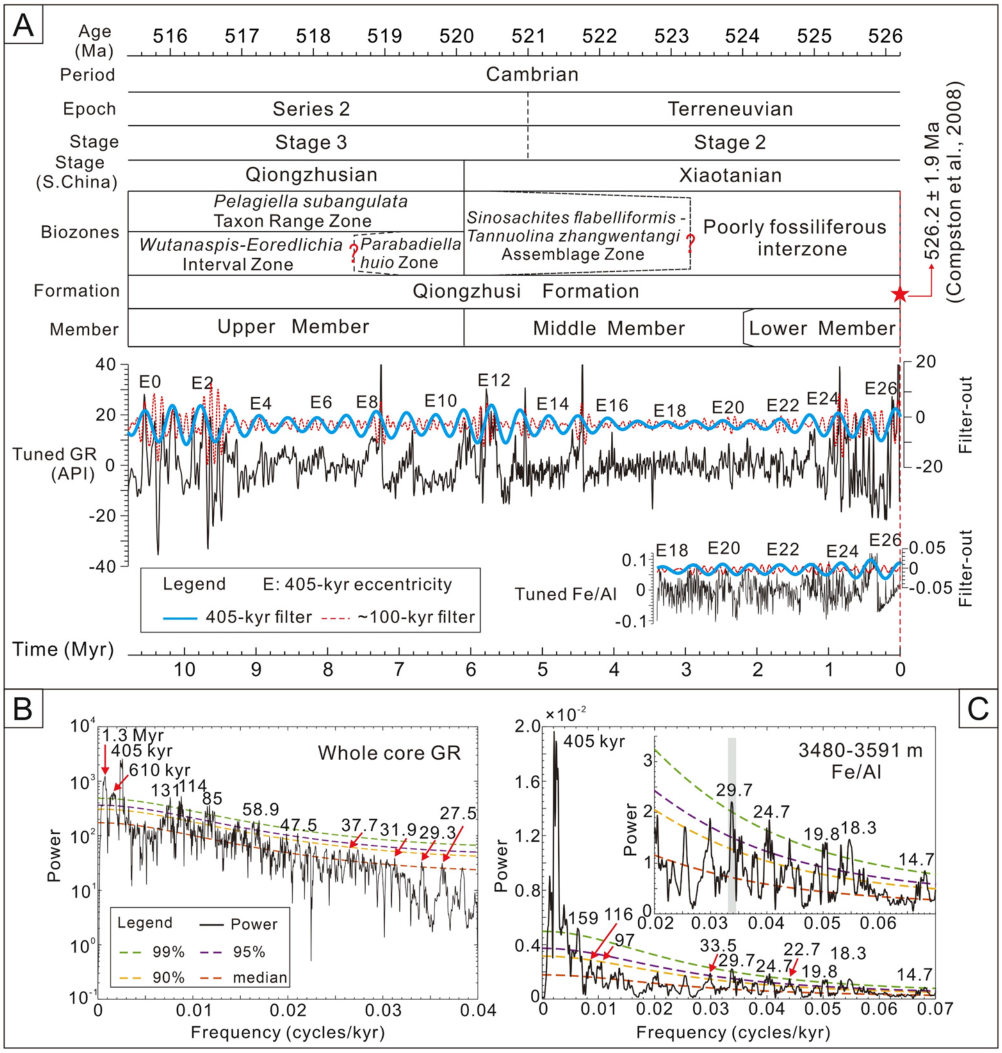

Fig. 6. (A) The astronomically tuned time scale for GR series, Fe/Al series and biozones of the Qiongzhusi Formation. Tuning was accomplished by assigning the filtered ~14.9-m cycles of the Lower and Middle Members and 11.6-m cycles of the Upper Member of the GR series as well as 14.0-m cycles of the Fe/Al series to the 405-kyr eccentricity cycles, respectively. The tuned GR and Fe/Al series and corresponding filtered 405-kyr and ~100-kyr cycles are shown (Gaussian filter, both passband: 0.00247 ± 0.0005 cycles/kyr and 0.01 ± 0.002 cycles/kyr, respectively). The base of the Cambrian Stage 3 is defined following the 521 Ma of the Geological Time Scale 2020 (Peng et al., 2020). Absolute time scale with the base of the Lower Member anchored to a 526.2 ± 1.9 Ma age of a thin tuff from the base of the Qiongzhusi Fm. in the Maidiping section (Compston et al., 2008). (B, C) 2π MTM power spectrum of the 405-tuned GR (B) and Fe/Al series from 3480 to 3591 m (C) at Well A. The gray area represents uncertainty for the main obliquity period of 29.7 kyr in the early Cambrian that likely results from the bandwidth resolution limit in the spectrum analysis (i.e., the uncertainty of ± Rayleigh frequency).

shift of net water balance between land and ocean are still hard to pinpoint. An estimated volume of 25×10^6 km^3 for global groundwater storage is generally equivalent to the estimated volume of 24×10^6 km^3 of ice currently on land and corresponds to a sea-level differential of ±76 m or ±50 m after isostatic adjustment (Hay and Leslie, 1990). Because of the late Cenozoic uplift, which caused severe erosion and stripping of a large amount of young and highly porous sediments formed in Asia and North America during the earlier Cenozoic Period, the current global groundwater volume may represent the minimum potential through geologic history (Hay and Leslie, 1990).

The early Cambrian is considered a greenhouse climate comparable to the late Cretaceous and early Paleocene warm period according to estimated mean annual sea surface temperatures calculated from δ^{18}O values of pristine phosphatic microfossils (Hearing et al., 2018). Because of lacking permanent polar ice sheets, the high-amplitude eustasy variations in the early Cambrian cannot be explained through the glacio-eustasy model. Although estimates of continental groundwater storage capacity in deep time are controversial (Davies et al., 2020), Peters and Husson (2015) suggest that the capacity during the early Cambrian may be equivalent to an over 330 ± 41 m difference in sea level. Accordingly, the total groundwater storage capacity in early Cambrian sediments may be sufficient to trigger the observed major global sea-level variations (>75 m) in the compilation of Phanerozoic sea-level change (Snedden and Liu, 2010).

Filtered ~1.5 Myr cycles of both DYNOT and ρ_1 are in antiphase with ~1.5 Myr obliquity modulation cycles of the tuned GR, probably further supporting a causal link between long-term Milankovitch cycles forcing and million-year scale sea-level change in the early Cambrian greenhouse (Fig. 8). The heat, moisture, and precipitation associated with meridional insolation gradients are expected to be significantly affected by obliquity cycle variations, as evidenced by a coupled ocean-atmosphere general circulation model and Pleistocene benthic δ^{18}O records (e.g., Huybers and Wunsch, 2005; Raymo and Nisancioglu, 2003). Changes in poleward moisture and heat transport dominated by long-term obliquity modulation cycles could have a significant impact on net variations in groundwater reserves (i.e., the amount of water available in the oceans), eventually raising or lowering sea level during

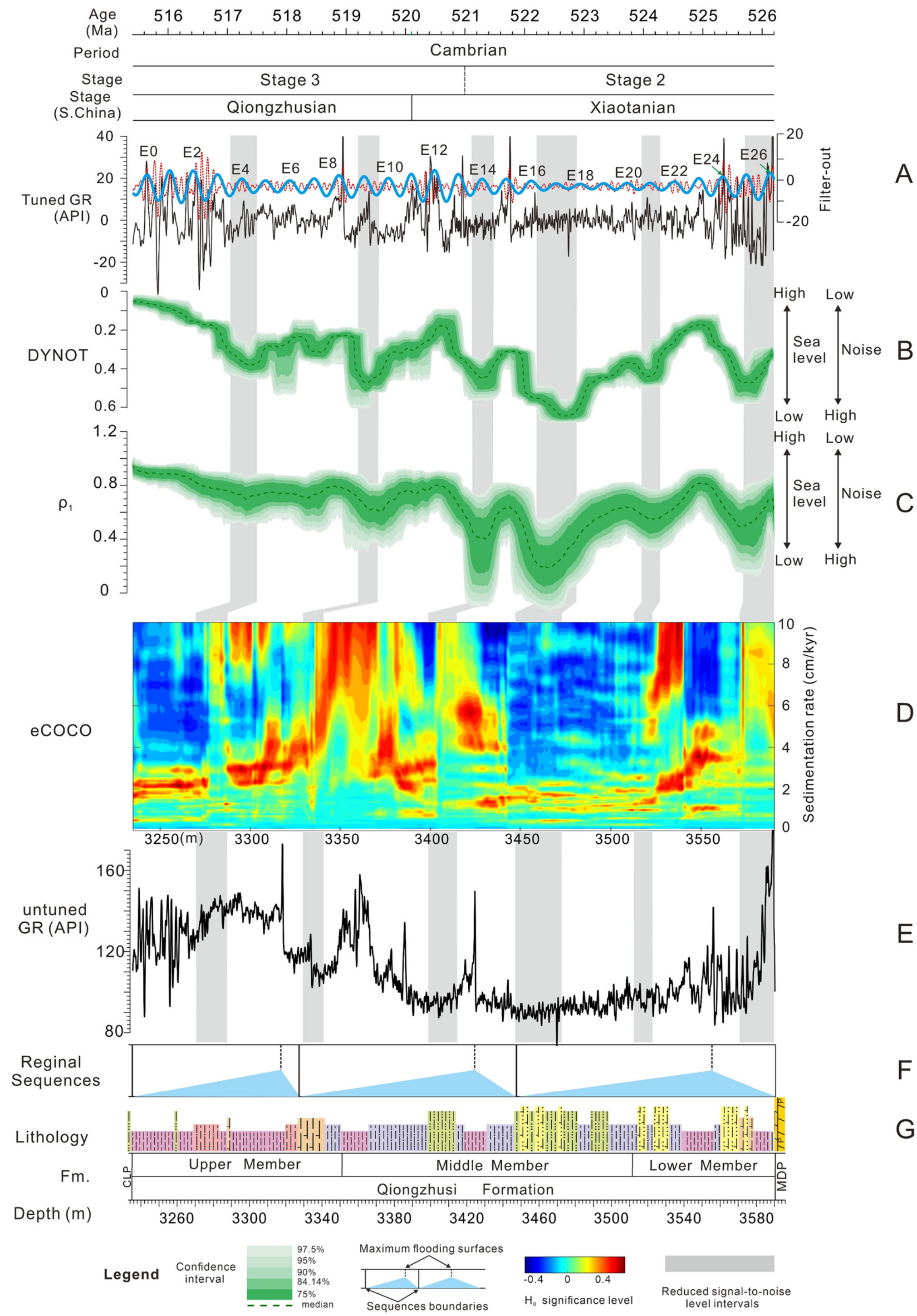

Fig. 7. Evaluation of the sedimentation noise model for reconstructing sea-level changes. (A) The 405-kyr tuned GR series from Fig. 6. (B, C) DYNOT and ρ_1 models of tuned GR series. (D) eCOCO sedimentation rate map from Fig. 5. (E) The untuned GR series of the whole Qiongzhusi Formation. (F) Regional sequences stratigraphy (Liu et al., 2018). (G) Lithological units of the Qiongzhusi Fm. of Well A. The DYNOT and ρ_1 models were calculated using a running window of 400 kyr. Confidence levels were estimated using a Monte Carlo analysis with 5000 iterations.

warm periods (Li et al., 2018a, 2016; Wang et al., 2020; Wendler and Wendler, 2016). During ~1.5 Myr obliquity modulation cycles maxima under the early Cambrian greenhouse, an enhanced poleward flux of moisture and heat will lead to high precipitation rates in the middle and high latitudes. An increased amount of water that penetrates into the aquifer results in rising continental aquifers storage; thereby, less water is available to the oceans, leading to lower sea levels. In contrast, at times of nodes in the ~1.5 Myr obliquity modulation, a less poleward transfer of moisture and heat could decrease precipitation falling on the high latitudes continents. Subsequently, less water is held by the continent aquifers, and more water returns to the oceans through evaporation and runoff, eventually raising the sea level.

Although the geochronology and patterns of rapid bio-evolutionary events for the Cambrian bio-radiation are still disputed and poorly constrained, it is commonly considered that biological innovation is likely promoted by atmospheric and oceanic oxygen level and modification of ocean environments (e.g., Chen

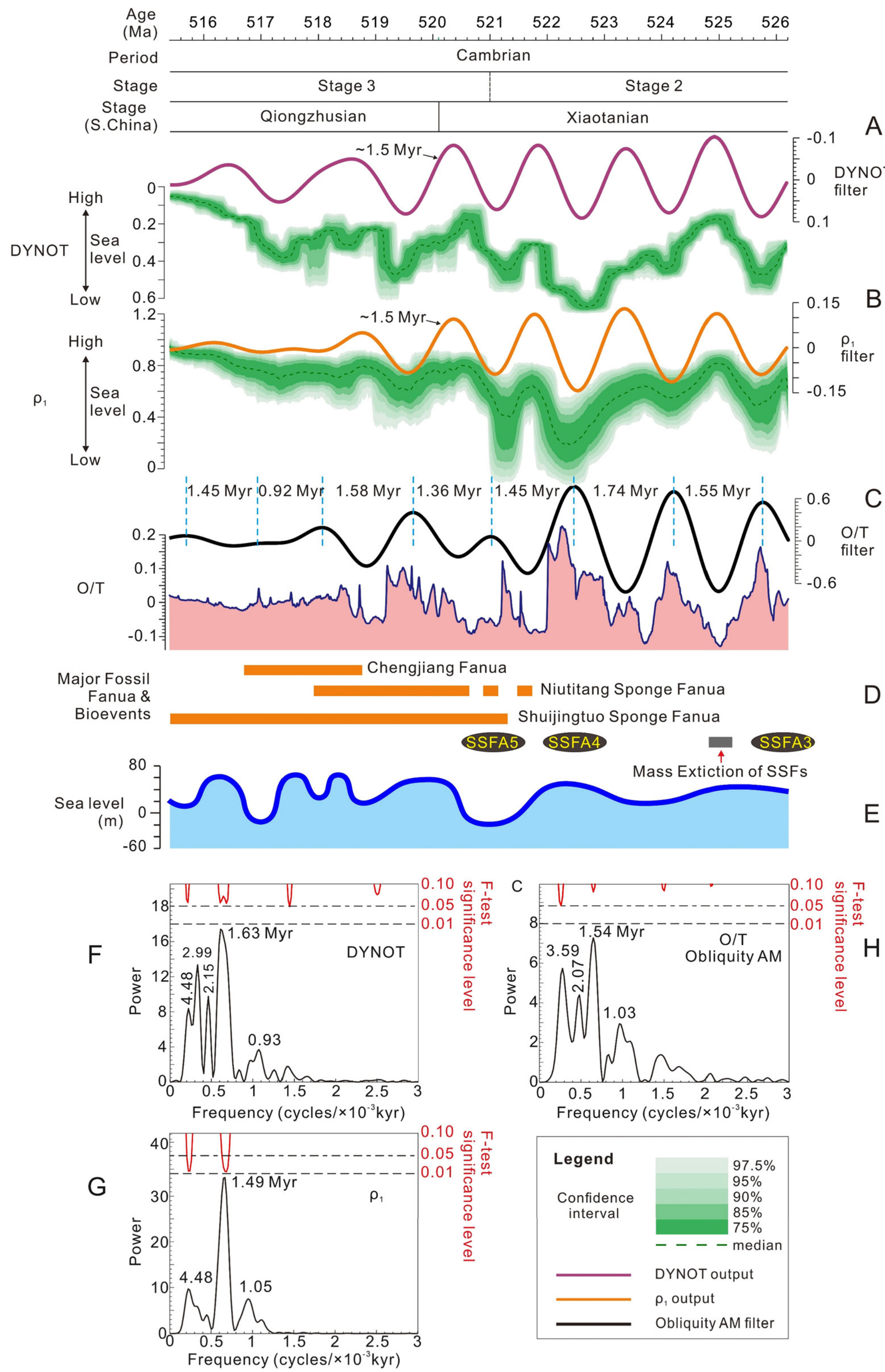

Fig. 8. Global sea level, obliquity cycles, major bioevents in the early Cambrian. (A, B) DYNOT and ρ_1 results of the 405 kyr-tuned GR series from Fig. 7 as well as ∼1.5 Myr cycles filter-output (passband: 0.0006 ± 0.0002 cycles/kyr) from DYNOT (purple line) and ρ_1 (orange line). (C) Observed O/T (blue line) and the filtered ∼1.5 Myr obliquity (black line) amplitude modulation cycles (passband: 0.0006 ± 0.0002 cycles/kyr) of the observed O/T models. (D) Major biological event during the "Cambrian explosion" (Peng et al., 2020); the appearance of small shelly fossils assemblages 3-5 is from Jin et al. (2016) and Steiner et al. (2007). (E) Global sea-level curve during the early Cambrian (after Snedden and Liu, 2010). Periodograms for the detrended median output by DYNOT (F) and ρ_1 (G) models, and detrended obliquity variance/total variance (O/T) (H) of the 405 kyr-tuned GR series from the Qiongzhusi Formation.

et al., 2015; Dahl et al., 2019; Sperling et al., 2013; Wei et al., 2018). Significantly, it appears that the occurrence of small shelly fossil assemblages 3-5 broadly coincides with ∼1.5 Myr modulation maxima and the lower sea-level period (Fig. 8). The probably invigorated nutrient cycles and ocean circulation in shallow-marine environments during the lower sea level may contribute to transient relatively high marine primary productivity and O_2 production episodes, thereby perhaps facilitating animal diversification (e.g., Kidder and Worsley, 2010, 2004; Wei et al., 2021). In fact, the overall temporal trends of intermittent biological recovery events after the end-Permian mass extinction roughly fit with the global sea level lower-stand and maxima in long-term obliquity cycles astronomical forcing (Hermann et al., 2012; Li et al., 2016). The mass extinction of small shelly fossils during the early Cambrian, by contrast, corresponds to an aquifer-eustatic transgression event driven by the ∼1.5 Myr obliquity variation minima (Fig. 8). This possibly suggests that the flooding of the shelves with H_2S anoxic bottom water and relatively higher sea surfaces temperature at low latitudes may be a potential trigger for the small shelly fossils biotic crisis. Similar mechanisms have also been considered to obstruct ecosystem restoration after the end-Permian biotic crisis (e.g., Kidder and Worsley, 2004; Knoll et al., 1996). These linkages between astronomically forced sea-level oscillations, environmental and climate change, and biological innovations during the early Cambrian greenhouse increase our understanding of the complex mechanisms and patterns of the current rising global sea level, warmer climate, biological response.

5.4. Implications for the chaotic behavior of the solar system and evolution of the Earth-Moon system

According to the numerical theoretical model, the Solar System has been considered chaotic (Laskar, 1989); thereby, the orbital parameters beyond 50 million years ago are not predicted accurately by astronomical solutions (Laskar et al., 2004). The chaotic motion of the Solar System is primarily governed by multiple secular resonances in the inner solar system, the critical component of which is the Earth-Mars secular resonance, characterized by the Myr-scale amplitude modulations (Laskar, 1990). These Myr-scale cycles associated with Earth-Mars secular resonance presently define a secular resonance of $(s_4 - s_3) - 2(g_4 - g_3) = 0$ (i.e., ∼2.4 Myr eccentricity: ∼1.2 Myr obliquity) and even evolve to libration in a new resonance $(s_4 - s_3) - (g_4 - g_3) = 0$, i.e., ∼1.2 Myr eccentricity: ∼1.2 Myr obliquity, where g_3 and g_4, as well as s_3 and s_4, are precession of the perihelion and the node of Earth and Mars, respectively (Laskar et al., 2004).

The $s_4 - s_3$ term and $g_4 - g_3$ term in the early Cambrian were extracted from the tuned GR series at Well A through evaluating the spectrum analysis of long eccentricity variance/total variance (E/T) and the amplitude modulation (AM) envelope curves of the 405 kyr cycles, and obliquity variance/total variance (O/T), respectively. The power spectrum of E/T reveals that the $s_4 - s_3$ term has a prominent periodicity of ∼1.50 Myr and subordinate periodicities of ∼4.90 Myr, 2.25 Myr, and 1.08 Myr for the Stage 2 to Stage 3 (Fig. 9E). The MTM power spectrum of the AM envelope curve of 405 kyr cycles displays a prominent peak at ∼1.50 Myr and subordinate peaks at ∼5.99 Myr, ∼2.57 Myr and 1.15 Myr, matching well with those in the power spectrum of E/T (Fig. 9F). The power spectrum of O/T indicates that the $g_4 - g_3$ term has a prominent periodicity of ∼1.54 Myr and subordinate periodicities of 3.59 Myr and 2.07 Myr, and 1.03 Myr (Fig. 8H). The filtered ∼1.5 Myr cycles from both E/T series and AM envelope curve of 405 kyr cycles are in phase with filtered ∼1.54 Myr cycles of 405 kyr-tuned GR series (Fig. 9A, B, and C), further supporting long period amplitude modulations of eccentricity cycles with the periodicity of ∼1.50 Myr cycles (i.e., $s_4 - s_3$ term) in the early Cambrian. The frequency modulation of eccentricity cycles associated with the Earth-Mars secular resonance has changed its periodicity throughout Earth history due to the chaotic nature of the Solar System, such as ∼2 Myr and ∼2.4 Myr cycles in the Cenozoic Era (e.g., Abels et al., 2010; De Vleeschouwer et al., 2017; Valero et al., 2014; van Dam et al., 2006), ∼1.6 Myr cycle in the early Cretaceous (e.g., Huang et al., 2010b), and ∼2.0 Myr and ∼1.8 Myr cycle in the late Jurassic (e.g., Huang et al., 2010a; Ikeda and Tada, 2020), ∼1.8 Myr and ∼1.6 Myr cycle in the late Triassic (e.g., Hüsing et al., 2011; Olsen, 2010, 1986; Sha et al., 2015) and the middle Triassic (e.g., Ikeda et al., 2010), 3.45 Myr cycle in the late Permian (Fang et al., 2015a; Wu et al., 2013a), ∼2.4 Myr, 1.6 Myr and 1.2 Myr cycle in the Carboniferous (e.g., Wu et al., 2019), ∼2.4 Myr, 2.0-2.5 Myr cyclesin the early and late Devonian (Da Silva et al., 2016; De Vleeschouwer et al., 2013), and ∼1.9 Myr and ∼2.4 Myr cycle in the middle and late Ordovician (e.g., Fang et al., 2019; Lu et al., 2019; Zhong et al., 2020, 2018). By comparison, $s_4 - s_3$ cycles are less often reported than $g_4 - g_3$ cycles. Previous studies revealed that the $s_4 - s_3$ cycles have a periodicity of 1.0- and 1.2-Myr cycles in the Cenozoic Era (e.g., Boulila et al., 2011; Pälike et al., 2006; van Dam et al., 2006), of 0.8-, 1.0-, 1.2- and 1.95-Myr cycles in the Mesozoic Era (e.g., Laurin et al., 2015; Li et al., 2016; Ma et al., 2019; Sha et al., 2015; Wu et al., 2013b), and of 1.0-, 1.2- and 3.11-Myr cycles in the Paleozoic Era (e.g., Da Silva et al., 2016; Fang et al., 2015b; Wu et al., 2019, 2013a; Zhong et al., 2018).

Thus, the ∼1.54 Myr and ∼1.5 Myr cycles in the amplitude modulation of obliquity and long eccentricity signals in gamma-ray logs (GR) of the Qiongzhusi Formation probably suggest a new resonance state between Earth and Mars (i.e., $(s_4 - s_3) - (g_4 - g_3) = 0$; ∼1.5 Myr eccentricity: ∼1.54 Myr obliquity) in the early Cambrian, as reported from the geological records in the late Carboniferous (Wu et al., 2019), the late Cretaceous (Ma et al., 2017) and the early Eocene (Westerhold et al., 2017). In addition, it should be noted that the frequency of these multi-Myr cycles in the geological record might be modulated by factors other than astronomical forcing, such as tectonic, volcanic processes, and non-linear responses within the Earth surface system, which may reduce the precision of the Myr-scale cycles extracted from the geological record. Thus, multiple independent studies of multi-Myr cycles in geologic records will be recommended to verify these results further. Collectively, our geologic evidence for these amplitude modulation cycles in the early Cambrian provides a fundamental limit to the possible chaotic behavior of the Solar System in deep time, especially Earth-Mars secular resonance.

An obliquity period of 29.6 ± 0.7 kyr at ∼524 Ma is observed from the MTM power spectrum of tuned Fe/Al series (Fig. 6C), where the uncertainty derives from the ± Rayleigh frequency of each spectrum peak induced by the bandwidth resolution limit (Thomson, 2011). This new estimate for the early Cambrian main obliquity period matches well with 31.4 ± 1.2 kyr at ∼493 Ma (Sørensen et al., 2020) and 30.7 ± 0.7 kyr at ∼500 Ma (Fang et al., 2020) and 32.3 ± 4.2 kyr at 524 Ma predicted by Waltham's model (Waltham, 2015). According to the $k + s_3$ approach (see Section 3.5.1), we calculate a precession constant k of 62.65 ± 1.04 arcsec/yr in the early Cambrian (∼524 Ma) using the Eq. (1) (See SI) and the obtained obliquity period of 29.6 ± 0.7 kyr. Then inputting the k value into Eq. (2), (3), (4) and (5) (See SI), we calculate an Earth-Moon distance of 368,200 ± 1,300 km and a day length of 21.29 ± 0.19 hr in the Early Cambrian (∼524 Ma).

Moreover, the Bayesian inversion approach (i.e., TimeOptMCMC) proposed by Meyers and Malinverno (2018) was employed to provide independent validation for reconstructing the history of Earth-Moon system characteristics. We have focused our analysis on the Qiongzhusi Fe/Al data between 3480 and 3520 m due to the high fidelity of the astronomical signal (Fig. S5 in SI). The TimeOptMCMC analysis results indicate a precession constant of 59.94 ± 0.25 arcsec/y (2σ; Fig. 10 and Fig. S7 in SI), an early Cambrian Earth-Moon distance of 371,650 ± 350 km and length of day of 21.80 ± 0.05 h (Fig. 10A, B).

According to the two independent astrochronologic approaches (i.e., $k + s_3$ and Bayesian inversion approaches; see Section 3.5), we obtain two different estimated values for the early Cambrian precession constant k, Earth-Moon distance, and day length. However,

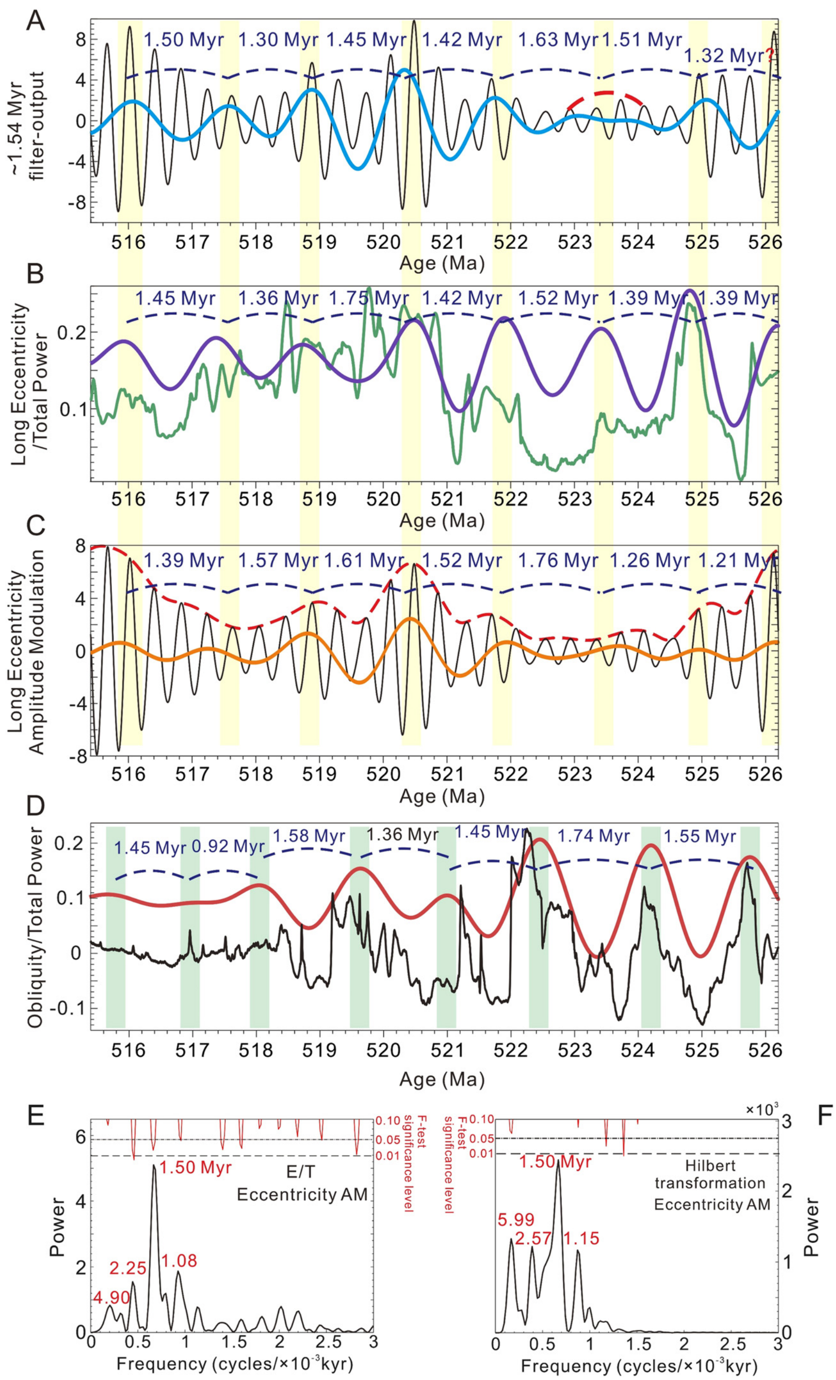

Fig. 9. A comparison of amplitude modulations expressed in the Qiongzhusi Formation long eccentricity signals. (A) the filtered ∼1.54-Myr cycles (blue line) and 405-kyr cycles (black line) were directly extracted from the 405-kyr tuned GR series (passband: 0.00065 ± 0.0002 cycles/kyr). (B) Long eccentricity/total power (green line) and filtered ∼1.5 Myr cycles (purple line) in the amplitude modulation of eccentricity signals (passband: 0.000675 ± 0.000225 cycles/kyr). (C) The amplitude modulation (red dash line) of the 405-kyr eccentricity cycle (black line) obtained by the Hilbert transform of the bandpass-filtered long eccentricity signal (passband: 0.00275 ± 0.00075 cycles/kyr) and the orange line represents the filtered ∼1.5 Myr cycles in the amplitude modulation of eccentricity signals (passband: 0.000625 ± 0.000225 cycles/kyr). (D) Obliquity /total power (black line) and filtered ∼1.5 Myr cycles (dark red line) in the amplitude modulation of obliquity signals from in Fig. 8C. (E, F) Periodograms of the amplitude modulation series in B and C. The approximately 1.5-Myr and 1.5-Myr cycles extracted from the long eccentricity and obliquity amplitude modulation are labeled with dashed arcs. Yellow boxes indicate locations when both long eccentricity assessments (A, B and C) show consistently high values. Green boxes indicate high values locations in obliquity amplitude modulation.

our new calculations are comparable with Earth-Moon distance of 371,000 ± 7,200 km and day length of 21.2 ± 0.94 hr at 524 Ma predicted by Waltham's model (Waltham, 2015; Fig. 10). These results reconstructed by $k + s_3$ and TimeOptMCMC approaches from the early Cambrian Qiongzhusi Formation are consistent with a continuous increase of tidal dissipation rate with time predicted by ocean models (Fig. 10C, Bills and Ray, 1999; Waltham, 2015). Thus, the lunar recession appears to be slower beyond 250 Ma ago but was roughly consistent with the present rate in the past 250 Myr (Fig. 10C, Bills and Ray, 1999; Laskar et al., 2004; Sørensen et al., 2020; Waltham, 2015). These empirical constraints on the evolution of the Earth-Moon system in the early Paleozoic enhance our knowledge of the chaotic dynamics of the solar system in deep time.

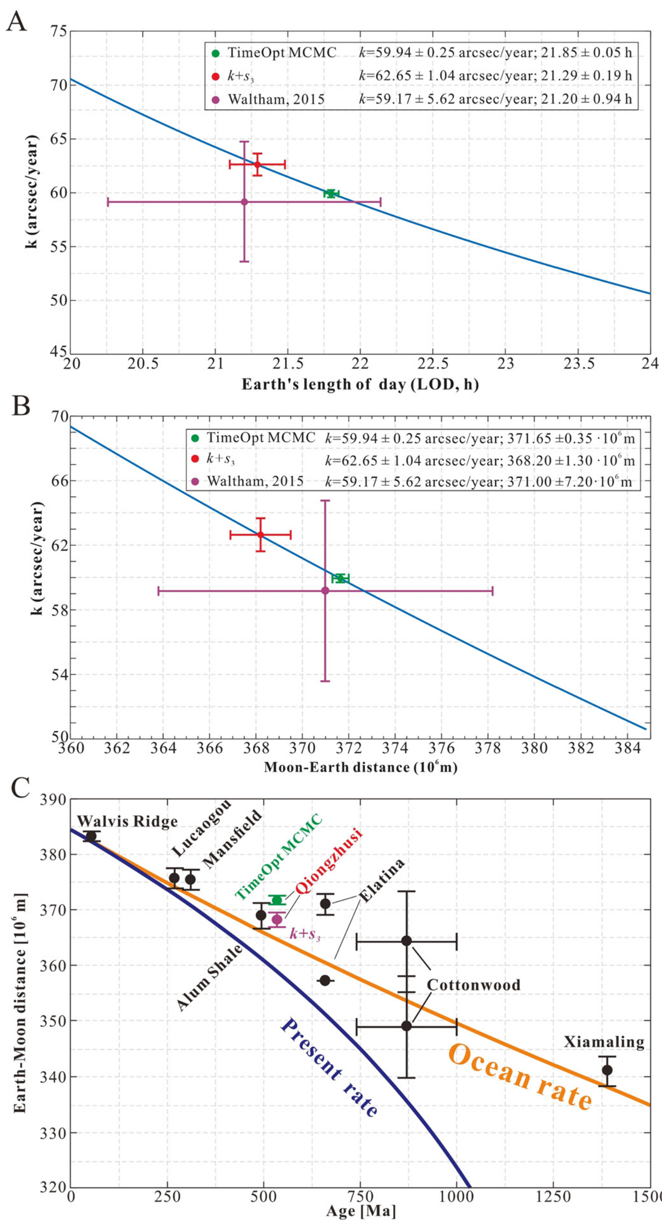

Fig. 10. TimeOptMCMC and $k + s_3$ methods reconstructed precession constant k, the Earth's length of day (LOD) (A) and Earth-Moon distance (B) based on the Qiongzhusi Fm. Fe/Al records in the early Cambrian, compared with the Waltham's model (2015) theoretical model, and the blue line is calculated using geodynamic equations in the SI (C). Evolution of the Earth-Moon distance and observed empirical constraints from geological records in the past 1500 Myr (modified from Sørensen et al., 2020). The Earth-Moon distance in the early Cambrian is calculated according to TimeOptMCMC (green dot) and $k + s_3$ (red dot) methods. The predicted current tidal dissipation rate (dark blue line) and the 'Ocean model' (orange line) from Waltham's model (2015) (see equations in the *SI*). The tabulated details and sources are summarized in the supplementary information (Table S3).

6. Conclusions

Four key findings have resulted from our cyclostratigraphic study of the Lower Cambrian Qiongzhusi Formation in South China:

We provide a ~10.8 Myr-long high-resolution astronomical time scale across Stage 2-Stage 3 by the astronomical tuning of gamma-ray logs and Fe/Al series to the stable 405-kyr long-eccentricity cycles. Our high-resolution astronomical time scale suggests a total duration of 6.09 ± 0.20 Myr for the poorly fossiliferous Zone and the *Sinosachites flabelliformis-Tannuolina zhangwentangi* Assemblage Zone and a duration of 4.70 ± 0.20 Myr for the *Pelagiella subangulata* Taxon Range Zone. The base of the Qiongzhusian Stage, defined by the earliest occurrence trilobites *Parabadiella huoi* (Biozone VII) in South China, is astrochronologically constrained at 520.11 ± 1.91 Ma, confirming that the earliest occurrence of trilobite in China is younger in age than those in Siberia and Laurentia.

(2) The sedimentary noise modeling of the 405-tuned GR series reveals sea-level changes in the early Cambrian greenhouse. The inferred sea-level curves are supported by the geological evidence of sequence stratigraphic interpretations, lithofacies stacking patterns, and the contemporaneously global sea-level change. Furthermore, intervals that sedimentation rate signals distort in the eCOCO results fit broadly with the enhanced sedimentary noise record and sequence stratigraphic boundaries.

(3) The Myr-scale eustasy in the early Cambrian greenhouse periods may be linked to land-ocean water exchange dominated by changes in poleward moisture and heat transport that are governed by ~1.5 Myr obliquity modulation cycles.

(4) This new modulation pattern (~1.5 Myr eccentricity: ~1.5 Myr obliquity) in the early Cambrian Stage 2-Stage 3, related to Earth-Mars secular resonance, could represent geological evidence for possible chaotic behavior of the Solar System in deep time. Application of two independent astrochronologic approaches to the Qiongzhusi Fm. Fe/Al series provides robust estimated values for the precession constant k, Earth-Moon distance, and a day length in the early Cambrian.

CRediT authorship contribution statement

Tan Zhang: Conceptualization, Methodology, Writing – original draft. **Yifan Li:** Conceptualization, Methodology, Writing – review & editing. **Tailiang Fan:** Writing – review & editing. **Anne-Christine Da Silva:** Writing – review & editing. **Juye Shi:** Writing – review & editing. **Qi Gao:** Data curation, Investigation. **Mingzhi Kuang:** Data curation, Investigation. **Wangwei Liu:** Data curation, Investigation. **Zhiqian Gao:** Writing – review & editing. **Mingsong Li:** Conceptualization, Methodology, Writing – review & editing.

Declaration of competing interest

The authors declare that they have no known competing financial interests or personal relationships that could have appeared to influence the work reported in this paper.

Acknowledgements

We thank Prof. K.P. Kodama, Prof. Tais W. Dahl and Editor Boswell Wing for thoughtful comments and constructive suggestions on this paper. This work is supported by the National Natural Science Foundation of China (Grants U19B6003-01-02, 41802155, 42072040, 41972130), the Fundamental Research Funds for the Central Universities (2-9-2019-265), Strategic Priority Research Program of the Chinese Academy of Sciences (Grant XDA14010201-02), and High-performance Computing Platform of Peking University.

Appendix A. Supplementary material

Supplementary material related to this article can be found online at https://doi.org/10.1016/j.epsl.2022.117420.

References

Abels, H.A., Aziz, H.A., Krijgsman, W., Smeets, S.J.B., Hilgen, F.J., 2010. Long-period eccentricity control on sedimentary sequences in the continental Madrid Basin

(middle Miocene, Spain). Earth Planet. Sci. Lett. 289, 220–231. https://doi.org/10.1016/j.epsl.2009.11.011.
Berger, A., Loutre, M.F., 1994. Astronomical forcing through geological time. In: Orbital Forcing and Cyclic Sequences. Blackwell Scientific Publications, Oxford, pp. 15–24.
Berger, A., Loutre, M.F., Laskar, J., 1992. Stability of the astronomical frequencies over the Earth's history for paleoclimate studies. Science 80 (255), 560–566. https://doi.org/10.1126/science.255.5044.560.
Bills, B.G., Ray, R.D., 1999. Lunar orbital evolution: a synthesis of recent results. Geophys. Res. Lett. 26, 3045–3048. https://doi.org/10.1029/1999GL008348.
Boulila, S., Galbrun, B., Miller, K.G., Pekar, S.F., Browning, J.V., Laskar, J., Wright, J.D., 2011. On the origin of Cenozoic and Mesozoic "third-order" eustatic sequences. Earth-Sci. Rev. 109, 94–112. https://doi.org/10.1016/j.earscirev.2011.09.003.
Brasier, M.D., Magaritz, M., Corfield, R., Huilin, L., Xiche, W., Lin, O., Zhiwen, J., Hamdi, B., Tinggui, H., Fraser, A.G., 1990. The carbon- and oxygen-isotope record of the Precambrian-Cambrian boundary interval in China and Iran and their correlation. Geol. Mag. https://doi.org/10.1017/S0016756800014886.
Chen, X., Ling, H.F., Vance, D., Shields-Zhou, G.A., Zhu, M., Poulton, S.W., Och, L.M., Jiang, S.Y., Li, D., Cremonese, L., Archer, C., 2015. Rise to modern levels of ocean oxygenation coincided with the Cambrian radiation of animals. Nat. Commun. 6. https://doi.org/10.1038/ncomms8142.
Cleveland, W.S., Devlin, S.J., 1988. Locally weighted regression: an approach to regression analysis by local fitting. J. Am. Stat. Assoc. 83, 596–610. https://doi.org/10.1080/01621459.1988.10478639.
Compston, W., Zhang, Z., Cooper, J.A., Ma, G., Jenkins, R.J.F., 2008. Further SHRIMP geochronology on the early Cambrian of South China. Am. J. Sci. 308, 399–420. https://doi.org/10.2475/04.2008.01.
Dahl, T.W., Connelly, J.N., Li, D., Kouchinsky, A., Gill, B.C., Porter, S., et al., 2019. Atmosphere-ocean oxygen and productivity dynamics during early animal radiations. Proc. Natl. Acad. Sci. USA 116 (39), 19352–19361. https://doi.org/10.1073/pnas.1901178116.
Da Silva, A.C., Hladil, J., Chadimová, L., Slavík, L., Hilgen, F.J., Bábek, O., Dekkers, M.J., 2016. Refining the Early Devonian time scale using Milankovitch cyclicity in Lochkovian–Pragian sediments (Prague Synform, Czech Republic). Earth Planet. Sci. Lett. 455, 125–139. https://doi.org/10.1016/j.epsl.2016.09.009.
Davies, A., Gréselle, B., Hunter, S.J., Baines, G., Robson, C., Haywood, A.M., Ray, D.C., Simmons, M.D., van Buchem, F.S.P., 2020. Assessing the impact of aquifer-eustasy on short-term Cretaceous sea-level. Cretac. Res. 112. https://doi.org/10.1016/j.cretres.2020.104445.
De Vleeschouwer, D., Rakociński, M., Racki, G., Bond, D.P.G., Sobień, K., Claeys, P., 2013. The astronomical rhythm of Late-Devonian climate change (Kowala section, Holy Cross Mountains, Poland). Earth Planet. Sci. Lett. 365, 25–37. https://doi.org/10.1016/j.epsl.2013.01.016.
De Vleeschouwer, D., Vahlenkamp, M., Crucifix, M., Pälike, H., 2017. Alternating Southern and Northern Hemisphere climate response to astronomical forcing during the past 35 m.y. Geology 45, 375–378. https://doi.org/10.1130/G38663.1.
Erwin, D.H., Laflamme, M., Tweedt, S.M., Sperling, E.A., Pisani, D., Peterson, K.J., 2011. The Cambrian conundrum: early divergence and later ecological success in the early history of animals. Science 80 (334), 1091–1097. https://doi.org/10.1126/science.1206375.
Fang, J., Wu, H., Fang, Q., Shi, M., Zhang, S., Yang, T., Li, H., Cao, L., 2020. Cyclostratigraphy of the global stratotype section and point (GSSP) of the basal Guzhangian Stage of the Cambrian Period. Palaeogeogr. Palaeoclimatol. Palaeoecol. 540, 109530. https://doi.org/10.1016/j.palaeo.2019.109530.
Fang, Q., Wu, H., Hinnov, L.A., Jing, X., Wang, X., Jiang, Q., 2015a. Geologic evidence for chaotic behavior of the planets and its constraints on the third-order eustatic sequences at the end of the Late Paleozoic Ice Age. Palaeogeogr. Palaeoclimatol. Palaeoecol. 440, 848–859. https://doi.org/10.1016/j.palaeo.2015.10.014.
Fang, Q., Wu, H., Hinnov, L.A., Jing, X., Wang, X., Jiang, Q., 2015b. Geologic evidence for chaotic behavior of the planets and its constraints on the third-order eustatic sequences at the end of the Late Paleozoic Ice Age. Palaeogeogr. Palaeoclimatol. Palaeoecol. 440, 848–859. https://doi.org/10.1016/j.palaeo.2015.10.014.
Fang, Q., Wu, H., Wang, X., Yang, T., Li, H., Zhang, S., 2019. An astronomically forced cooling event during the Middle Ordovician. Glob. Planet. Change 173, 96–108. https://doi.org/10.1016/j.gloplacha.2018.12.010.
Gale, A.S., Hardenbol, J., Hathway, B., Kennedy, W.J., Young, J.R., Phansalkar, V., 2002. Global correlation of Cenomanian (Upper Cretaceous) sequences: evidence for Milankovitch control on sea level. Geology 30, 291–294. https://doi.org/10.1130/0091-7613(2002)030<0291:GCOCUC>2.0.CO;2.
Geyer, G., 1996. The Moroccan fallotaspidid trilobites revisited. Beringeria 18, 89–199.
Geyer, G., Landing, E., 2006. Latest Ediacaran and Cambrian of the Moroccan Atlas regions. In: Ediacaran–Cambrian Depos. Environ. Stratigr. West. Atlas Reg., pp. 7–46.
Geyer, G., Repina, L.N., Zhuravlev, A.Y., 1990. Correlation along the Lower/Middle Cambrian boundary–a puzzling story with an elusory end. In: Tretij mezhdunarodnyj Simp. po kembrijskoj Sist. Tezisy Dokl., pp. 100–102.
Harvey, T.H.P., Williams, M., Condon, D.J., Wilby, P.R., Siveter, D.J., Rushton, A.W.A., Leng, M.J., Gabbott, S.E., 2011. A refined chronology for the Cambrian succession of southern Britain. J. Geol. Soc. Lond. 168, 705–716. https://doi.org/10.1144/0016-76492010-031.
Hay, W.W., Leslie, M.A., 1990. Could possible changes in global groundwater reservoir cause eustatic sea-level change in the structure of the ocean. In: Sea-Level Chang, pp. 161–170.
Hays, J.D., Imbrie, J., Shackleton, N.J., 1976. Variations in the Earth's orbit: pacemaker of the ice ages. Science 80 (194), 1121–1132. https://doi.org/10.1126/science.194.4270.1121.
Hearing, T.W., Harvey, T.H.P., Williams, M., Leng, M.J., Lamb, A.L., Wilby, P.R., Gabbott, S.E., Pohl, A., Donnadieu, Y., 2018. An early Cambrian greenhouse climate. Sci. Adv. 4, eaar5690. https://doi.org/10.1126/sciadv.aar5690.
Hermann, E., Hochuli, P.A., Bucher, H., Roohi, G., 2012. Uppermost Permian to Middle Triassic palynology of the Salt Range and Surghar Range, Pakistan. Rev. Palaeobot. Palynol. 169, 61–95. https://doi.org/10.1016/j.revpalbo.2011.10.004.
Hinnov, L.A., 2013. Cyclostratigraphy and its revolutionizing applications in the Earth and planetary sciences. Bull. Geol. Soc. Am. 125, 1703–1734. https://doi.org/10.1130/B30934.1.
Hinnov, L.A., 2018. Cyclostratigraphy and Astrochronology in 2018, Stratigraphy & Timescales. Elsevier Ltd.
Hinnov, L.A., Hilgen, F.J., 2012. Cyclostratigraphy and astrochronology. Geol. Time Scale 2012, 63–83. https://doi.org/10.1016/B978-0-444-59425-9.00004-4.
Hollingsworth, J.S., 2007. Fallotaspidoid trilobite assemblage (Lower Cambrian) from the Esmeralda Basin (western Nevada, U.S.A.): the oldest trilobites from Laurentia. Alcheringa Ann. Australas J. Palaeontol. 31, 123–140. https://doi.org/10.1080/03115510701586897.
Hollingsworth, J.S., 2011. Lithostratigraphy and biostratigraphy of Cambrian Stage 3 in Western Nevada and Eastern California. Mus. North. Ariz. Bull. 67, 26–42.
Huang, C., Hesselbo, S.P., Hinnov, L., 2010a. Astrochronology of the late Jurassic Kimmeridge Clay (Dorset, England) and implications for Earth system processes. Earth Planet. Sci. Lett. 289, 242–255. https://doi.org/10.1016/j.epsl.2009.11.013.
Huang, C., Hinnov, L., Fischer, A.G., Grippo, A., Herbert, T., 2010b. Astronomical tuning of the Aptian Stage from Italian reference sections. Geology 38, 899–902. https://doi.org/10.1130/G31177.1.
Huang, H., Gao, Y., Jones, M.M., Tao, H., Carroll, A.R., Ibarra, D.E., Wu, H., Wang, C., 2020. Astronomical forcing of Middle Permian terrestrial climate recorded in a large paleolake in northwestern China. Palaeogeogr. Palaeoclimatol. Palaeoecol. 550, 109735. https://doi.org/10.1016/j.palaeo.2020.109735.
Hüsing, S.K., Deenen, M.H.L., Koopmans, J.G., Krijgsman, W., 2011. Magnetostratigraphic dating of the proposed Rhaetian GSSP at Steinbergkogel (Upper Triassic, Austria): implications for the Late Triassic time scale. Earth Planet. Sci. Lett. 302, 203–216. https://doi.org/10.1016/j.epsl.2010.12.012.
Huybers, P., Wunsch, C., 2005. Obliquity pacing of the late Pleistocene glacial terminations. Nature 434, 491–494. https://doi.org/10.1038/nature03401.
Ikeda, M., Tada, R., 2020. Reconstruction of the chaotic behavior of the solar system from geologic records. Earth Planet. Sci. Lett. 537, 116168. https://doi.org/10.1016/j.epsl.2020.116168.
Ikeda, M., Tada, R., Sakuma, H., 2010. Astronomical cycle origin of bedded chert: a middle Triassic bedded chert sequence, Inuyama, Japan. Earth Planet. Sci. Lett. 297, 369–378. https://doi.org/10.1016/j.epsl.2010.06.027.
Jiang, G., Wang, X., Shi, X., Xiao, S., Zhang, S., Dong, J., 2012. The origin of decoupled carbonate and organic carbon isotope signatures in the early Cambrian (ca. 542–520 Ma) Yangtze platform. Earth Planet. Sci. Lett. 317–318, 96–110. https://doi.org/10.1016/j.epsl.2011.11.018.
Jin, C., Li, C., Algeo, T.J., Planavsky, N.J., Cui, H., Yang, X., Zhao, Y., Zhang, X., Xie, S., 2016. A highly redox-heterogeneous ocean in South China during the early Cambrian (∼529-514 Ma): implications for biota-environment co-evolution. Earth Planet. Sci. Lett. 441, 38–51. https://doi.org/10.1016/j.epsl.2016.02.019.
Kidder, D.L., Worsley, T.R., 2004. Causes and consequences of extreme Permo-Triassic warming to globally equable climate and relation to the Permo-Triassic extinction and recovery. Palaeogeogr. Palaeoclimatol. Palaeoecol. 203, 207–237. https://doi.org/10.1016/S0031-0182(03)00667-9.
Kidder, D.L., Worsley, T.R., 2010. Phanerozoic Large Igneous Provinces (LIPs), HEATT (Haline Euxinic Acidic Thermal Transgression) episodes, and mass extinctions. Palaeogeogr. Palaeoclimatol. Palaeoecol. 295, 162–191. https://doi.org/10.1016/j.palaeo.2010.05.036.
Knoll, A.H., Bambach, R.K., Canfield, D.E., Grotzinger, J.P., 1996. Comparative Earth history and Late Permian mass extinction. Science 80 (273), 452–457. https://doi.org/10.1126/science.273.5274.452.
Kodama, K.P., Hinnov, L.A., 2014. Rock Magnetic Cyclostratigraphy, Rock Magnetic Cyclostratigraphy. John Wiley & Sons.
Lamy, Klump, Hebbeln, Wefer, 2000. Late Quaternary rapid climate change in northern Chile. Terra Nova 12, 8–13. https://doi.org/10.1046/j.1365-3121.2000.00265.x.
Landing, E., Geyer, G., Brasier, M.D., Bowring, S.A., 2013. Cambrian Evolutionary Radiation: context, correlation, and chronostratigraphy—overcoming deficiencies of the first appearance datum (FAD) concept. Earth-Sci. Rev. 123, 133–172. https://doi.org/10.1016/j.earscirev.2013.03.008.
Laskar, J., 1989. A numerical experiment on the chaotic behaviour of the Solar System. Nature 338, 237–238. https://doi.org/10.1038/338237a0.
Laskar, J., 1990. The chaotic motion of the solar system: a numerical estimate of the size of the chaotic zones. Icarus 88, 266–291. https://doi.org/10.1016/0019-1035(90)90084-M.

Laskar, J., Robutel, P., Joutel, F., Gastineau, M., Correia, A.C.M., Levrard, B., 2004. A long-term numerical solution for the insolation quantities of the Earth. Astron. Astrophys. 428, 261–285. https://doi.org/10.1051/0004-6361:20041335.

Laskar, J., Gastineau, M., Delisle, J.-B., Farrés, A., Fienga, A., 2011. Strong chaos induced by close encounters with Ceres and Vesta. Astron. Astrophys. 532, L4. https://doi.org/10.1051/0004-6361/201117504.

Laurin, J., Meyers, S.R., Uličný, D., Jarvis, I., Sageman, B.B., 2015. Axial obliquity control on the greenhouse carbon budget through middle- to high-latitude reservoirs. Paleoceanography 30, 133–149. https://doi.org/10.1002/2014PA002736.

Li, M., Huang, C., Hinnov, L., Ogg, J., Chen, Z.Q., Zhang, Y., 2016. Obliquity-forced climate during the Early Triassic hothouse in China. Geology 44, 623–626. https://doi.org/10.1130/G37970.1.

Li, M., Zhang, Y., Huang, C., Ogg, J., Hinnov, L., Wang, Y., Zou, Z., Li, L., 2017. Astronomical tuning and magnetostratigraphy of the Upper Triassic Xujiahe formation of South China and Newark Supergroup of North America: implications for the Late Triassic time scale. Earth Planet. Sci. Lett. 475, 207–223. https://doi.org/10.1016/j.epsl.2017.07.015.

Li, M., Hinnov, L.A., Huang, C., Ogg, J.G., 2018a. Sedimentary noise and sea levels linked to land-ocean water exchange and obliquity forcing. Nat. Commun. 9, 1004. https://doi.org/10.1038/s41467-018-03454-y.

Li, M., Kump, L.R., Hinnov, L.A., Mann, M.E., 2018b. Tracking variable sedimentation rates and astronomical forcing in Phanerozoic paleoclimate proxy series with evolutionary correlation coefficients and hypothesis testing. Earth Planet. Sci. Lett. 501, 165–179. https://doi.org/10.1016/j.epsl.2018.08.041.

Li, M., Hinnov, L., Kump, L., 2019a. Acycle: time-series analysis software for paleoclimate research and education. Comput. Geosci. 127, 12–22. https://doi.org/10.1016/j.cageo.2019.02.011.

Li, M., Huang, C., Ogg, J., Zhang, Y., Hinnov, L., Wu, H., Chen, Z.Q., Zou, Z., 2019b. Paleoclimate proxies for cyclostratigraphy: comparative analysis using a Lower Triassic marine section in South China. Earth-Sci. Rev. 189, 125–146. https://doi.org/10.1016/j.earscirev.2019.01.011.

Liu, D., Huang, C., Kemp, D.B., Li, M., Ogg, J.G., Yu, M., Foster, W.J., 2021. Paleoclimate and sea level response to orbital forcing in the Middle Triassic of the eastern Tethys. Glob. Planet. Change 199, 103454. https://doi.org/10.1016/j.gloplacha.2021.103454.

Liu, Y., Huang, C., Ogg, J.G., Algeo, T.J., Kemp, D.B., Shen, W., 2019. Oscillations of global sea-level elevation during the Paleogene correspond to 1.2-Myr amplitude modulation of orbital obliquity cycles. Earth Planet. Sci. Lett. 522, 65–78. https://doi.org/10.1016/j.epsl.2019.06.023.

Liu, Z., Du, W., Gao, B., Hu, Z., Zhang, Y., Wu, J., Fen, D., 2018. Sedimentary model and distribution of organic-rich shale in the sequence stratigraphic framework: a case study of Lower Cambrian in Upper Yangtze Region. Earth Sci. Ed. 48, 1–14. https://doi.org/10.13278/j.cnki.jjuese.20160265.

Lu, Yangbo, Huang, C., Jiang, S., Zhang, J., Lu, Yongchao, Liu, Y., 2019. Cyclic late Katian through Hirnantian glacioeustasy and its control of the development of the organic-rich Wufeng and Longmaxi shales, South China. Palaeogeogr. Palaeoclimatol. Palaeoecol. 526, 96–109. https://doi.org/10.1016/j.palaeo.2019.04.012.

Ma, C., Meyers, S.R., Sageman, B.B., 2017. Theory of chaotic orbital variations confirmed by Cretaceous geological evidence. Nature 542, 468–470. https://doi.org/10.1038/nature21402.

Ma, C., Meyers, S.R., Sageman, B.B., 2019. Testing Late Cretaceous astronomical solutions in a 15 million year astrochronologic record from North America. Earth Planet. Sci. Lett. 513, 1–11. https://doi.org/10.1016/j.epsl.2019.01.053.

Maloof, A.C., Ramezani, J., Bowring, S.A., Fike, D.A., Porter, S.M., Mazouad, M., 2010. Constraints on early Cambrian carbon cycling from the duration of the Nemakit-Daldynian–Tommotian boundary δ13C shift, Morocco. Geology 38, 623–626. https://doi.org/10.1130/G30726.1.

Mann, M.E., Lees, J.M., 1996. Robust estimation of background noise and signal detection in climatic time series. Clim. Change 33, 409–445. https://doi.org/10.1007/BF00142586.

Meyers, S.R., 2015. The evaluation of eccentricity-related amplitude modulation and bundling in paleoclimate data: an inverse approach for astrochronologic testing and time scale optimization. Paleoceanography 30, 1625–1640. https://doi.org/10.1002/2015PA002850.

Meyers, S.R., 2021. Astrochron: an R package for astrochronology.

Meyers, S.R., Malinverno, A., 2018. Proterozoic Milankovitch cycles and the history of the solar system. Proc. Natl. Acad. Sci. 115, 6363–6368. https://doi.org/10.1073/pnas.1717689115.

Miller, K.G., 2005. The Phanerozoic record of global sea-level change. Science 80 (310), 1293–1298. https://doi.org/10.1126/science.1116412.

Mou, C., Liang, W., Zhou, K., Ge, X., Kang, J., Chen, X., 2012. Sedimentary facies and palaeogeography of the middle-upper Yangtze area during the Early Cambrian (Terreneuvian-Series 2). Sediment. Geol. Tethyan Geol. 32, 41–53.

Mudelsee, M., Bickert, T., Lear, C.H., Lohmann, G., 2014. Cenozoic climate changes: a review based on time series analysis of marine benthic δ18O records. Rev. Geophys. 52, 333–374. https://doi.org/10.1002/2013RG000440.

Naish, T., Powell, R., Levy, R., Wilson, G., Scherer, R., 2009. Obliquity-paced Pliocene West Antarctic ice sheet oscillations. Nature 458, 322–328. https://doi.org/10.1038/nature07867.

Olsen, P.E., 1986. A 40-million-year lake record of early Mesozoic orbital climatic forcing. Science 80 (234), 842–848. https://doi.org/10.1126/science.234.4778.842.

Olsen, P.E., 2010. Fossil Great Lakes of the Newark supergroup - 30 years later. In: Field Trip Guidebook, 83rd Annual Meeting New York State Geological Association. Citeseer, pp. 101–162.

Olsen, P.E., Laskar, J., Kent, D.V., Kinney, S.T., Reynolds, D.J., Sha, J., Whiteside, J.H., 2019. Mapping solar system chaos with the Geological Orrery. Proc. Natl. Acad. Sci. USA 166, 10664–10673. https://doi.org/10.1073/pnas.1813901116.

Omar, H., Da Silva, A.-C., Yaich, C., 2021. Linking the variation of sediment accumulation rate to short term sea-level change using cyclostratigraphy: case study of the Lower Berriasian Hemipelagic Sediments in Central Tunisia (Southern Tethys). Front. Earth Sci. 9, 176. https://doi.org/10.3389/feart.2021.638441.

Pälike, H., Norris, R.D., Herrle, J.O., Wilson, P.A., Coxall, H.K., Lear, C.H., Shackleton, N.J., Tripati, A.K., Wade, B.S., 2006. The heartbeat of the Oligocene climate system. Science 80 (314), 1894–1898. https://doi.org/10.1126/science.1133822.

Pattan, J.N., Parthiban, G., Gupta, S.M., Mir, I.A., 2012. Fe speciation and Fe/Al ratio in the sediments of southeastern Arabian Sea as an indicator of climate change. Quat. Int. 250, 19–26. https://doi.org/10.1016/j.quaint.2011.08.007.

Peng, S., Babcock, L.E., Cooper, R.A., 2012. The Cambrian Period. In: Geologic Time Scale 2012. Elsevier.

Peng, S.C., Babcock, L.E., Ahlberg, P., 2020. The Cambrian Period. In: Geologic Time Scale 2020. Elsevier, pp. 565–629.

Peters, S., Husson, J., 2015. Phanerozoic growth of the epicontinental sedimentary reservoir: implications for long-term sea level change. In: AGU Fall Meeting, pp. PP33B–2307.

R Core Team 2021. R: A language and environment for statistical computing.

Raiswell, R., Canfield, D.E., 2012. The iron biogeochemical cycle past and present. Geochem. Perspect. 1, 1–232. https://doi.org/10.7185/geochempersp.1.1.

Raymo, M.E., Nisancioglu, K., 2003. The 41 kyr world: Milankovitch's other unsolved mystery. Paleoceanography 18. https://doi.org/10.1029/2002pa000791.

Saker-Clark, M., Kemp, D.B., Coe, A.L., 2019. Portable X-ray fluorescence spectroscopy as a tool for cyclostratigraphy. Geochem. Geophys. Geosyst. 20, 2531–2541. https://doi.org/10.1029/2018GC007582.

Sames, B., Wagreich, M., Wendler, J.E., Haq, B.U., Conrad, C.P., Melinte-Dobrinescu, M.C., Hu, X., Wendler, I., Wolfgring, E., Yilmaz, I., Zorina, S.O., 2016. Review: short-term sea-level changes in a greenhouse world — a view from the Cretaceous. Palaeogeogr. Palaeoclimatol. Palaeoecol. 441, 393–411. https://doi.org/10.1016/j.palaeo.2015.10.045.

Schnyder, J., Ruffell, A., Deconinck, J.F., Baudin, F., 2006. Conjunctive use of spectral gamma-ray logs and clay mineralogy in defining late Jurassic-early Cretaceous palaeoclimate change (Dorset, U.K.). Palaeogeogr. Palaeoclimatol. Palaeoecol. 229, 303–320. https://doi.org/10.1016/j.palaeo.2005.06.027.

Sha, J., Olsen, P.E., Pan, Y., Xu, D., Wang, Y., Zhang, X., Yao, X., Vajda, V., 2015. Triassic-Jurassic climate in continental high-latitude Asia was dominated by obliquity-paced variations (Junggar Basin, Ürümqi, China). Proc. Natl. Acad. Sci. USA 112, 3624–3629. https://doi.org/10.1073/pnas.1501137112.

Shackleton, N.J., Hagelberg, T.K., Crowhurst, S.J., 1995. Evaluating the success of astronomical tuning: pitfalls of using coherence as a criterion for assessing pre-Pleistocene timescales. Paleoceanography 10, 693–697. https://doi.org/10.1029/95PA01454.

Shergold, J.H., Rozanov, A.Y., Palmer, A.R., 1991. The Cambrian system on the Siberian platform. Int. Union Geol. Sci. Publ. Trondheim 133.

Snedden, J.W., Liu, C., 2010. A compilation of Phanerozoic sea-level change, coastal onlaps and recommended sequence designations. Am. Assoc. Pet. Geol. Bull.

Sørensen, A.L., Nielsen, A.T., Thibault, N., Zhao, Z., Schovsbo, N.H., Dahl, T.W., 2020. Astronomically forced climate change in the late Cambrian. Earth Planet. Sci. Lett. 548, 116475. https://doi.org/10.1016/j.epsl.2020.116475.

Sperling, E.A., Frieder, C.A., Raman, A.V., Girguis, P.R., Levin, L.A., Knoll, A.H., 2013. Oxygen, ecology, and the Cambrian radiation of animals. Proc. Natl. Acad. Sci. USA 110, 13446–13451. https://doi.org/10.1073/pnas.1312778110.

Steiner, M., Li, G., Qian, Y., Zhu, M., Erdtmann, B.D., 2007. Neoproterozoic to Early Cambrian small shelly fossil assemblages and a revised biostratigraphic correlation of the Yangtze Platform (China). Palaeogeogr. Palaeoclimatol. Palaeoecol. 254, 67–99. https://doi.org/10.1016/j.palaeo.2007.03.046.

Sui, Y., Huang, C., Zhang, R., Wang, Z., Ogg, J., 2019. Astronomical time scale for the middle-upper Doushantuo formation of Ediacaran in South China: implications for the duration of the Shuram/Wonoka negative δ13C excursion. Palaeogeogr. Palaeoclimatol. Palaeoecol. 532, 109273. https://doi.org/10.1016/j.palaeo.2019.109273.

Thomson, D.J., 2011. Time–series analysis of paleoclimate data. In: Encyclopedia of Paleoclimatology and Ancient Environments. Springer, Netherlands, Dordrecht, pp. 949–959.

Valero, L., Garcés, M., Cabrera, L., Costa, E., Sáez, A., 2014. 20 Myr of eccentricity paced lacustrine cycles in the Cenozoic Ebro Basin. Earth Planet. Sci. Lett. 408, 183–193. https://doi.org/10.1016/j.epsl.2014.10.007.

van Dam, J.A., Abdul Aziz, H., Ángeles Álvarez Sierra, M., Hilgen, F.J., van den Hoek Ostende, L.W., Lourens, L.J., Mein, P., van der Meulen, A.J., Pelaez-Campomanes, P., 2006. Long-period astronomical forcing of mammal turnover. Nature 443, 687–691. https://doi.org/10.1038/nature05163.

Varlamov, A.I., Rozova, A.V., Khamentovsky, Y., 2008. The Zhurinsky Mys section. Cambr. Syst. Sib. Platform. Part 1 Aldan-Lena Reg. In: XIII Int. F. Conf. Cambr. Stage Subdiv. Work. Gr., pp. 71–92.
Waltham, D., 2015. Milankovitch period uncertainties and their impact on cyclostratigraphy. J. Sediment. Res. 85, 990–998. https://doi.org/10.2110/jsr.2015.66.
Wang, J., Li, Z.X., 2003. History of neoproterozoic rift basins in South China: implications for Rodinia break-up. Precambrian Res. 122, 141–158. https://doi.org/10.1016/S0301-9268(02)00209-7.
Wang, M., Chen, H., Huang, C., Kemp, D.B., Xu, T., Zhang, H., Li, M., 2020. Astronomical forcing and sedimentary noise modeling of lake-level changes in the Paleogene Dongpu Depression of North China. Earth Planet. Sci. Lett. 535, 116116. https://doi.org/10.1016/j.epsl.2020.116116.
Wang, M., Li, M., Kemp, D.B., Boulila, S., Ogg, J.G., 2022. Sedimentary noise modeling of lake-level change in the Late Triassic Newark Basin of North America. Glob. Planet. Change 208, 103706. https://doi.org/10.1016/j.gloplacha.2021.103706.
Wei, G.Y., Planavsky, N.J., Tarhan, L.G., Chen, X., Wei, W., Li, D., Ling, H.F., 2018. Marine redox fluctuation as a potential trigger for the Cambrian explosion. Geology 46, 587–590. https://doi.org/10.1130/G40150.1.
Wei, G.Y., Planavsky, N.J., He, T., Zhang, F., Stockey, R.G., Cole, D.B., Lin, Y.B., Ling, H.F., 2021. Global marine redox evolution from the late Neoproterozoic to the early Paleozoic constrained by the integration of Mo and U isotope records. Earth-Sci. Rev. 214, 103506. https://doi.org/10.1016/j.earscirev.2021.103506.
Wei, H., Shen, J., Schoepfer, S.D., Krystyn, L., Richoz, S., Algeo, T.J., 2015. Environmental controls on marine ecosystem recovery following mass extinctions, with an example from the Early Triassic. Earth-Sci. Rev. 149, 108–135. https://doi.org/10.1016/j.earscirev.2014.10.007.
Wendler, J.E., Wendler, I., 2016. What drove sea-level fluctuations during the mid-Cretaceous greenhouse climate? Palaeogeogr. Palaeoclimatol. Palaeoecol. 441, 412–419. https://doi.org/10.1016/j.palaeo.2015.08.029.
Wendler, J.E., Wendler, I., Vogt, C., Kuss, J., 2016. Link between cyclic eustatic sea-level change and continental weathering: evidence for aquifer-eustasy in the Cretaceous. Palaeogeogr. Palaeoclimatol. Palaeoecol. 441, 430–437. https://doi.org/10.1016/j.palaeo.2015.08.014.
Westerhold, T., Röhl, U., Frederichs, T., Agnini, C., Raffi, I., Zachos, J.C., Wilkens, R.H., 2017. Astronomical calibration of the Ypresian timescale: implications for seafloor spreading rates and the chaotic behavior of the solar system? Clim. Past 13, 1129–1152. https://doi.org/10.5194/cp-13-1129-2017.
Williams, G.E., 2000. Geological constraints on the Precambrian history of Earth's rotation and the moon's orbit. Rev. Geophys. 38, 37–59. https://doi.org/10.1029/1999RG900016.
Wu, H., Zhang, S., Hinnov, L.A., Jiang, G., Feng, Q., Li, H., Yang, T., 2013a. Time-calibrated Milankovitch cycles for the late Permian. Nat. Commun. 4, 1–8. https://doi.org/10.1038/ncomms3452.
Wu, H., Zhang, S., Jiang, G., Hinnov, L., Yang, T., Li, H., Wan, X., Wang, C., 2013b. Astrochronology of the Early Turonian-Early Campanian terrestrial succession in the Songliao Basin, northeastern China and its implication for long-period behavior of the Solar System. Palaeogeogr. Palaeoclimatol. Palaeoecol. 385, 55–70. https://doi.org/10.1016/j.palaeo.2012.09.004.
Wu, H., Fang, Q., Wang, X., Hinnov, L.A., Qi, Y., Shen, S., Yang, T., Li, H., Chen, J., Zhang, S., 2019. An ∼34 m.y. astronomical time scale for the uppermost Mississippian through Pennsylvanian of the Carboniferous System of the Paleo-Tethyan realm. Geology 47, 83–86. https://doi.org/10.1130/G45461.1.
Yang, B., Steiner, M., Keupp, H., 2015. Early Cambrian palaeobiogeography of the Zhenba-Fangxian Block (South China): independent terrane or part of the Yangtze Platform? Gondwana Res. 28, 1543–1565. https://doi.org/10.1016/j.gr.2014.09.020.
Yang, C., Li, X.H., Zhu, M., Condon, D.J., Chen, J., 2018. Geochronological constraint on the Cambrian Chengjiang Biota, South China. J. Geol. Soc. Lond. 175, 659–666. https://doi.org/10.1144/jgs2017-103.
Yin, R., Xu, L., Lehmann, B., Lepak, R.F., Hurley, J.P., Mao, J., Feng, X., Hu, R., 2017. Anomalous Mercury enrichment in Early Cambrian black shales of South China: Mercury isotopes indicate a seawater source. Chem. Geol. 467, 159–167. https://doi.org/10.1016/j.chemgeo.2017.08.010.
Zhang, X., Shu, D., Han, J., Zhang, Z., Liu, J., Fu, D., 2014. Triggers for the Cambrian explosion: hypotheses and problems. Gondwana Res. 25, 896–909. https://doi.org/10.1016/j.gr.2013.06.001.
Zhang, X., Ahlberg, P., Babcock, L.E., Choi, D.K., Geyer, G., Gozalo, R., Stewart Hollingsworth, J., Li, G., Naimark, E.B., Pegel, T., Steiner, M., Wotte, T., Zhang, Z., 2017. Challenges in defining the base of Cambrian Series 2 and Stage 3. Earth-Sci. Rev. 172, 124–139. https://doi.org/10.1016/j.earscirev.2017.07.017.
Zhong, Y., Li, Y., Zhang, X., Liu, S., Wu, F., Liu, D., Deng, X., Chen, S., Yang, F., Li, X., Jiang, B., 2014. Evolution characteristics of Central Sichuan palaeouplift and its relationship with early Cambrian Mianyang-Changning intracratonic sag. J. Chengdu Univ. Technol. (Sci. Technol. Ed.) 41, 703–712. https://doi.org/10.3969/i.issn.1671-9727.2014.06.05.
Zhong, Y., Wu, H., Zhang, Y., Zhang, S., Yang, T., Li, H., Cao, L., 2018. Astronomical calibration of the Middle Ordovician of the Yangtze Block, South China. Palaeogeogr. Palaeoclimatol. Palaeoecol. 505, 86–99. https://doi.org/10.1016/j.palaeo.2018.05.030.
Zhong, Y., Wu, H., Fan, J., Fang, Q., Shi, M., Zhang, S., Yang, T., Li, H., Cao, L., 2020. Late Ordovician obliquity-forced glacio-eustasy recorded in the Yangtze Block, South China. Palaeogeogr. Palaeoclimatol. Palaeoecol. 540, 109520. https://doi.org/10.1016/j.palaeo.2019.109520.
Zhu, G., Wang, P., Li, T., Zhao, K., Yan, H., Li, J., Zhou, L., 2021. Nitrogen geochemistry and abnormal Mercury enrichment of shales from the lowermost Cambrian Niutitang Formation in South China: implications for the marine redox conditions and hydrothermal activity. Glob. Planet. Change 199, 103449. https://doi.org/10.1016/j.gloplacha.2021.103449.
Zhu, M., Yang, A., Yuan, J., Li, G., Zhang, J., Zhao, F., Ahn, S.Y., Miao, L., 2019. Cambrian integrative stratigraphy and timescale of China. Sci. China Earth Sci. 62, 25–60. https://doi.org/10.1007/s11430-017-9291-0.